

©Copyright 2014

Irma Lam



# Feature Engineering for 3D Medical Image Applications

Irma Lam

A dissertation  
submitted in partial fulfillment of the  
requirements for the degree of

Doctor of Philosophy

University of Washington

2014

Reading Committee:

Linda Shapiro, Chair

Michael Cunningham

Su-In Lee

Program Authorized to Offer Degree:  
Biomedical and Health Informatics, School of Medicine

UMI Number: 3631883

All rights reserved

INFORMATION TO ALL USERS

The quality of this reproduction is dependent upon the quality of the copy submitted.

In the unlikely event that the author did not send a complete manuscript and there are missing pages, these will be noted. Also, if material had to be removed, a note will indicate the deletion.



UMI 3631883

Published by ProQuest LLC (2014). Copyright in the Dissertation held by the Author.

Microform Edition © ProQuest LLC.

All rights reserved. This work is protected against unauthorized copying under Title 17, United States Code



ProQuest LLC.  
789 East Eisenhower Parkway  
P.O. Box 1346  
Ann Arbor, MI 48106 - 1346



University of Washington

**Abstract**

Feature Engineering for 3D Medical Image Applications

Irma Lam

Chair of the Supervisory Committee:

Professor Linda Shapiro

Computer Science and Engineering

Feature engineering, including input representation, feature design, evaluation, and optimization, is essential to success in machine learning. For unstructured data like images and texts, feature engineering can often become the bottleneck in learning related tasks. Selecting the most effective and descriptive features can improve performance, proficiency, and precision in quantification applications, or enhance a good classifier in classification. Features are domain-specific. In order to express input explicitly, automatically, fully, yet intuitively, substantial knowledge of the applications and the nature of the input is often required to decide what features to use and to optimize the design. This thesis introduces a new set of feature engineering algorithms for medical research of 3D CT skull images in understanding craniosynostosis disorder. Three related tasks: 1) classification using 3D computed tomography scans of skulls, 2) severity assessment and class ranking, and 3) pre-post surgery change are used to demonstrate the effectiveness of the features and the algorithms that produce them.

Craniosynostosis, a disorder in which one or more fibrous joints of the skull fuse prematurely, causes skull deformity and is associated with increased intracranial pressure and developmental delays. In order to perform medical research studies that relate phenotypic abnormalities to outcomes such as cognitive ability or results of surgery, biomedical researchers need an automated methodology for quantifying the degree of abnormality of the disorder. While several papers have attempted this quantification through statistical mod-

els, the methods have not been intuitive to biomedical researchers and clinicians who want to use them. The goal of this work was to develop a general set of features upon which new quantification measures could be developed and tested. The features reported in this study were developed as basic shape measures, both single-valued and vector-valued, that are extracted from a projection-based plane of the 3D skull. This technique allows us to process images that would otherwise be eliminated in previous systems due to poor resolution, noise or imperfections on their original older CT scans.

- We test our new features on classification tasks and also compare their performance to previous research. In spite of their simplicity, the classification accuracy of our new features is significantly higher than previous results on head CT scan data from the same research studies.
- We propose a set of features derived from CT scans of the skull that can be used to quantify the degree of abnormality of the disorder. A thorough set of experiments is used to evaluate the features as compared to two human craniofacial experts in a ranking evaluation.
- We study pre-post surgery change based on selected features we use in quantifying the severity of deformity of the disorder. Using the same selected features, we also compare and contrast post-surgery craniosynostosis skulls to the unaffected class.

## TABLE OF CONTENTS

	Page
List of Figures . . . . .	iii
List of Tables . . . . .	viii
Glossary . . . . .	ix
Chapter 1: Introduction . . . . .	1
Chapter 2: Related Work . . . . .	5
2.1 Local, curvature discrepancy from normality and fusion index . . . . .	5
2.2 Feature-invariant image registration . . . . .	6
2.3 Three-dimensional vector analysis . . . . .	6
2.4 Symbolic signatures . . . . .	7
2.5 Azimuth-elevation-angle histogram . . . . .	7
2.6 Euclidian distance matrix . . . . .	7
2.7 Sparse logistic regression models . . . . .	8
2.8 Classifying by visual inspection . . . . .	9
2.9 Euclidean distance matrix analysis of facial morphology . . . . .	9
2.10 Landmark-based adapted geometric morphometrics . . . . .	10
2.11 Dense surface-modeling of facial morphology . . . . .	11
Chapter 3: Approach and methodology . . . . .	12
3.1 Data acquisition and preprocessing . . . . .	12
3.2 3D mesh region of interest extraction and re-orientation . . . . .	14
3.3 2D external contour point extraction from each 3D mesh . . . . .	15
3.4 Aggregate and low-level feature extraction . . . . .	16
3.5 Tasks . . . . .	21
Chapter 4: Classification Experiments and Results . . . . .	24
4.1 Classify abnormal as compared to controls . . . . .	24



4.2	Classify two and multi-abnormal as compared to each other . . . . .	25
4.3	Discussion . . . . .	26
Chapter 5:	Severity Assessment and Class Ranking Experiments and Results . . . . .	29
5.1	Clinician ranking orders . . . . .	29
5.2	Correlations and ranking comparisons . . . . .	29
5.3	Discussion . . . . .	38
Chapter 6:	Pre-post Surgery Change Effect Experiments and Results . . . . .	40
6.1	Metopic class . . . . .	40
6.2	Sagittal class . . . . .	44
6.3	Right unilateral subclass . . . . .	49
6.4	Left unilateral subclass . . . . .	55
6.5	Discussion . . . . .	57
Chapter 7:	Discussion, Conclusion, and Future Work . . . . .	59
7.1	Study limitations and challenges . . . . .	59
7.2	Conclusions . . . . .	60
7.3	Future work . . . . .	61
Bibliography	. . . . .	63

## LIST OF FIGURES

Figure Number	Page
1.1 Top is the posterior and bottom is the anterior of a skull. Also shown are the four main sutures of the calvarial vault. . . . .	2
1.2 Shapes of unaffected (left), sagittal, uni-coronal and metopic synostosis skulls. . . . .	3
2.1 Imperfections like holes, rings and noise as seen on some older CT scans can make processing and shape analysis difficult. . . . .	8
3.1 Flow chart of our system. Step A <i>Data Acquisition and Preprocessing</i> is not part of the automated system being developed. . . . .	13
3.2 Identifying the base plane based on the nasion and opisthion anatomical landmark points. This base plane was used as one x-y-z coordinate plane to re-orient the entire extracted 3D ROI. . . . .	14
3.3 Extracting a 2D external contour (right) by first projecting the 3D surface mesh (left) onto a 2D plane (middle). Keeping only the exterior points from the silhouette. This approach allows processing and shape analysis to be done even on older CT scans that have noise and challenging imperfections. . . . .	15
3.4 Original image with both nasion and opisthion anatomical landmark points in blue (left). Removing all vertices below the base plane to obtain the extracted ROI (right). The contour (yellow line on right) is rescaled and translated so that it shares the same center and bounds as the ROI. . . . .	15
3.5 By using the Procrustes method [1] [2] [3], a mean (or average) contour is computed from our 34 unaffected skull dataset. Each white line represents a contour of an unaffected skull in the 34 dataset; whereas the red line represents the averaged contour of the entire unaffected group. This red line is identical to the green lines in Fig. 3.6 . . . . .	16
3.6 (right) A more mean-unaffected like skull and (left) a less mean-unaffected like skull. The green lines on both images are identical. The green line represents the mean contour of the entire unaffected class contour. The white lines on both figures represent two contours from two different skulls. . . . .	17
3.7 (left) A less circular skull; (right) a more circular skull. . . . .	18
3.8 Illustration of a symmetrical sagittal synostosis skull (left) and an asymmetrical unilateral coronal synostosis skull (right). . . . .	19

3.9	(left) Left and right front-center contours, which fan 45 degree from the horizontal x-axis, are shown in magenta. Left and right front-tip contours, which fan 20 degree from the vertical front y-axis, are shown in cyan; (right) left and right back contours, which fan 45 degree from the vertical back y-axis, are shown in cyan. . . . .	20
3.10	(left) Components of the Angle vector at two different segment points along a contour: front-center segment contour in magenta and front-tip segment contour in cyan; (right) <i>change of average slope angle towards front tip</i> (COA) of this more deformed metopic skull is 27.38 degree. . . . .	21
3.11	(left) Components of the Angle vector at two different segment points along a contour: front-center segment contour in magenta and front-tip segment contour in cyan; (right) <i>change of average slope angle towards front tip</i> (COA) of this less deformed metopic skull is 40.93 degree. . . . .	22
3.12	The more deformed a sagittal skull is, the more angular its back angles are. (left) this more deformed sagittal skull has <i>average slope angle of back</i> at 56.959 degree; (right) this less deformed sagittal skull has <i>average slope angle of back</i> at 42.291 degree. . . . .	22
5.1	Illustration of a more shape-deformed metopic skull (left), which has less angular change at the front of a skull and a more persistent sharp angle towards the front tip, than a less shape-deformed metopic skull (right), whose contour gradually reduces in angular sharpness towards the front tip. . . . .	30
5.2	The 5 most shape-deformed of the total 25 metopic skulls. The 25th was the most severe skull and 24th was the second to the most. COA and front were machine ranked based on features that have demonstrated high correlation to ranks provided by the two human experts. . . . .	31
5.3	5 metopic least shape-deformed skulls. . . . .	31
5.4	5 metopic inconsistently ranked skulls . . . . .	32
5.5	Ranking orders provided by the two experts in correlation to machine ranking measure, COA. . . . .	33
5.6	Illustration of a more shape-deformed sagittal skull (left), whose back is more angular, its width over length ratio is lower, and as a whole, it is less circular; whereas a less shape-deformed sagittal skull (right), whose back is less angular and as a whole, it is more circular and appears more like the mean control skull representation. . . . .	33
5.7	5 sagittal most shape-deformed ranks. Back, cmp2Circle and cmp2Mean are machine ranked based on features that have demonstrated high correlation to ranking orders from the two experts. . . . .	34
5.8	5 sagittal least shape-deformed ranks. . . . .	35
5.9	5 sagittal inconsistently ranked skulls. . . . .	35

5.10	5 right unilateral coronal most shape-deformed ranks. <i>cmp2Mean</i> , <i>w2l</i> and symmetry are machine ranked based on features that have demonstrated higher correlation to ranking orders from the two experts. . . . .	37
5.11	5 right unilateral coronal least shape-deformed ranks. . . . .	38
6.1	The low and high bounds of features <i>cmp2Mean</i> , <i>w2l</i> , <i>cmp2Circle</i> , and <i>symmetry</i> in the unaffected class. . . . .	41
6.2	The low and high bounds of features <i>front</i> , <i>back</i> , and <i>COA</i> in the unaffected class. . . . .	41
6.3	Horizontal axis indicates the deformity ranks, where 1 is the least and 15 is the most severe according to the scoring feature of <i>change of average slope angle towards front tip (COA)</i> in the metopic synostosis class. . . . .	42
6.4	Horizontal axis indicates the deformity ranks, where 1 is the least and 15 is the most severe according to the scoring feature of <i>average slope angle of front tip (front)</i> in the metopic synostosis class. . . . .	43
6.5	5 metopic most shape-deformed pre-surgery skulls according to their <i>COA</i> features scores. Pre-post change effects according to features <i>COA</i> and <i>front</i> . . . . .	43
6.6	Vertical axis indicates the deformity measures according to the scoring feature of <i>change of average slope angle towards front tip (COA)</i> in the unaffected, the metopic post-surgery, and the metopic pre-surgery skulls. The grey shaded box shows where the deformity scores were out of the normal range. Note that all the pre-surgery skulls were out of the normal range. . . . .	44
6.7	Vertical axis indicates the deformity measures according to the scoring feature of <i>average slope angle of front tip (front)</i> in the unaffected, the metopic post-surgery, and the metopic pre-surgery skulls. The grey shaded box shows where the deformity scores were out of the normal range. Note that all the pre-surgery skulls were out of the normal range. . . . .	45
6.8	Horizontal axis indicates the deformity ranks, where 1 is the least and 21 is the most severe according to the scoring feature of <i>average slope angle of back (back)</i> in the sagittal class. . . . .	46
6.9	Horizontal axis indicates the deformity ranks, where 1 is the least and 21 is the most severe according to the scoring feature of <i>compare to circle (cmp2Circle)</i> in the sagittal class. . . . .	47
6.10	Horizontal axis indicates the deformity ranks, where 1 is the least and 21 is the most severe according to the scoring feature of <i>compare to mean unaffected (cmp2Mean)</i> in the sagittal class. . . . .	47
6.11	Horizontal axis indicates the deformity ranks, where 1 is the least and 21 is the most severe according to the scoring feature of <i>width to length ratio (w2l)</i> in the sagittal class. . . . .	48

6.12	5 sagittal most shape-deformed pre-surgery skulls according to their <i>back</i> features scores. Score changes of features <i>back</i> , <i>cmp2Circle</i> , <i>cmp2Mean</i> , and <i>w2l</i> from each of these 5 pre-surgery skulls to its 2-year post-surgery status. . . . .	48
6.13	Vertical axis indicates the deformity measures according to the scoring feature of <i>average slope angle of back (back)</i> in the unaffected, the sagittal post-surgery, and the sagittal pre-surgery skulls. The grey shaded box shows where the deformity scores were out of the normal range. Note that almost all the pre-surgery skulls were out of the normal range. . . . .	50
6.14	Vertical axis indicates the deformity measures according to the scoring feature of <i>compare to circle (cmp2Circle)</i> in the unaffected, the sagittal post-surgery, and the sagittal pre-surgery skulls. The grey shaded box shows where the deformity scores were out of the normal range. Note that almost all the pre-surgery skulls were out of the normal range. . . . .	50
6.15	Vertical axis indicates the deformity measures according to the scoring feature of <i>compare to mean unaffected (cmp2Mean)</i> in the unaffected, the sagittal post-surgery, and the sagittal pre-surgery skulls. The grey shaded box shows where the deformity scores were out of the normal range. Note that almost half of the pre-surgery skulls were out of the normal range. . . . .	51
6.16	Vertical axis indicates the deformity measures according to the scoring feature of <i>width to length ratio (w2l)</i> in the unaffected, the sagittal post-surgery, and the sagittal pre-surgery skulls. The grey shaded box shows where the deformity scores were out of the normal range. Note that majority of the pre-surgery skulls were out of the normal range. . . . .	51
6.17	Horizontal axis indicates the deformity ranks, where 1 is the least and 12 is the most severe according to the scoring feature of <i>compare to mean unaffected (cmp2Mean)</i> in right unilateral coronal subclass. . . . .	52
6.18	Horizontal axis indicates the deformity ranks, where 1 is the least and 12 is the most severe according to the scoring feature of <i>symmetry</i> in right unilateral coronal subclass. . . . .	53
6.19	Horizontal axis indicates the deformity ranks, where 1 is the least and 12 is the most severe according to the scoring feature of <i>width to length ratio (w2l)</i> in right unilateral coronal subclass. . . . .	53
6.20	5 right unilateral coronal most shape-deformed pre-surgery skulls according to their <i>cmp2Mean</i> features scores. Score changes of features <i>cmp2Mean</i> , <i>symmetry</i> , and <i>w2l</i> from each of these 5 pre-surgery skulls to its 2-year post-surgery status. . . . .	54

6.21	Vertical axis indicates the deformity measures according to the scoring feature of <i>compare to mean unaffected</i> ( <i>cmp2Mean</i> ) in the unaffected, the right uni-coronal post-surgery, and the right uni-coronal pre-surgery skulls. The grey shaded box shows where the deformity scores were out of the normal range. Note that half of the pre-surgery skulls were out of the normal range. . . . .	55
6.22	Vertical axis indicates the deformity measures according to the scoring feature of <i>symmetry</i> in the unaffected, the right uni-coronal post-surgery, and the right uni-coronal pre-surgery skulls. The grey shaded box shows where the deformity scores were out of the normal range. Note that more than half of the pre-surgery skulls were out of the normal range. . . . .	56
6.23	Vertical axis indicates the deformity measures according to the scoring feature of <i>width to length ratio</i> ( <i>w2l</i> ) in the unaffected, the right uni-coronal post-surgery, and the right uni-coronal pre-surgery skulls. The grey shaded box shows where the deformity scores were out of the normal range. Note that one third of the pre-surgery skulls were out of the normal range. . . . .	56
6.24	Horizontal axis indicates the deformity ranks, where 1 is the least and 9 is the most severe according to the scoring feature of <i>compare to mean unaffected</i> ( <i>cmp2Mean</i> ) in left unilateral coronal subclass. . . . .	57
6.25	Vertical axis indicates the deformity measures according to the scoring feature of <i>compare to mean unaffected</i> ( <i>cmp2Mean</i> ) in the unaffected, the left uni-coronal post-surgery, and the left uni-coronal pre-surgery skulls. The grey shaded box shows where the deformity scores were out of the normal range. Note that two of the pre-surgery skulls were out of the normal range. . . . .	58

## LIST OF TABLES

Table Number	Page
4.1 Accuracy with standard deviation of using each descriptor (column) individually to distinguish each affected skull dataset (row) from 34 unaffected skulls. . . . .	24
4.2 Accuracy with standard deviation of using each descriptor (column) collectively to distinguish each affected skull dataset (row) from 34 unaffected skulls.	25
4.3 Accuracy of comparison to previous results [4]. C is coronal. M is metopic. S is sagittal. . . . .	26
5.1 Correlation coefficients of metopic ranking orders. . . . .	30
5.2 Correlation coefficients of sagittal ranking orders. . . . .	34
5.3 Correlation results of uni-coronal ranking orders. . . . .	36
5.4 Correlation results of right uni-coronal ranking orders. . . . .	37
5.5 Correlation results of left uni-coronal ranking orders. . . . .	37

## GLOSSARY

CLUSTERING LASSO: a generalization of lasso that is designed for problems with highly correlated features whose correlations are too complicated to specify.

CRANIOSYNOSTOSIS: a condition in which one or more of the fibrous sutures in an infant skull prematurely fuses by turning into bone (ossification), thereby changing the growth pattern of the skull.

DEFORMATIONAL PLAGIOCEPHALY: DP, a postnatal flattening of the back of the skull.

DICOM: Digital Imaging and Communications in Medicine standard.

FEATURE LEARNING: to automatically learn a good representation of the input from unlabeled data instead of hand-engineering feature representation.

FUSED LASSO: a generalization of the lasso that is designed for problems with features that can be ordered in some meaningful way.

LASSO: a regression method that involves penalizing the absolute size of the regression coefficients.

LOGISTIC REGRESSION: a type of regression analysis used for predicting the outcome of a categorical dependent variable (a dependent variable that can take on a limited number of categories) based on one or more predictor variables.

METOPIC SYNOSTOSIS: synostosis in which the affected suture is between the frontal bones.



PROCRUSTES ANALYSIS: a form of statistical shape analysis, by optimally translating, rotating and uniformly scaling the objects in order to preserve shape for comparison.

SAGITTAL SYNOSTOSIS: synostosis in which the affected suture is between the parietal bones.

SVM: support vector machine, a family of supervised learning models with associated learning algorithms that analyze data and recognize patterns, used for classification and regression analysis.

UNILATERAL CORONAL SYNOSTOSIS: synostosis in which the affected suture is between the frontal and the parietal bones on either the right side or the left side of the skull.

WEKA: Waikato Environment for Knowledge Analysis is an open source software suite of machine learning written in Java, developed at the University of Waikato, New Zealand.

## ACKNOWLEDGMENTS

The author wishes to express deep gratitude to University of Washington, where she has had the opportunity to learn and perform research projects in the intersection of computer vision, craniosynostosis disorder and machine learning, and especially to my advisor Linda Shapiro for her funding support, exceptional mentorship, commitment to high quality output, generosity in her time, precision in judgement, and knowledge in our fields; to Seattle Children’s Research Institute for their datasets, teaching, guidance, and opportunities to collaborate and publish results with, and especially to Dr. Matthew Speltz, Dr. Michael Cunningham, Dr. Craig Birgfeld, and Sharman Conner; and to the National Library of Medicine and Biomedical and Health Informatics for their funding support; to the Multimedia Group in Computer Science and Engineering for their friendship and research ideas. The author also wants to thank her mother, her two daughters, her brother, her friends and extended family for their encouragement. Above all, the author is humbled in front of God for this life and all the blessings, experiences, trials, and opportunities that are entrusted to her.

## DEDICATION

To my dear mother, SukFong Pau, who has taught me what I need to know to survive;  
to my dear daughters, Wilma and Irena, because of them, my life is whole and new again.

## Chapter 1

### INTRODUCTION

It has been said if people could gain perfect clarity in high dimensions, machine learning would not be necessary. On one hand, the human impression is typically drawn from the three-dimensional world, in which human cognitive perception can often become fatigued and confused, even while processing data that is only three-dimensional. On the other hand, many problems we try to solve have far higher dimensional attributes than just three. Adding more to the complexity, raw data is typically not in a learnable form; therefore, features in the realm of machine learning must be first understood clearly by humans, then designed iteratively, and finally extracted selectively before they can be successfully utilized in problem solving. Thus, rather than analyzing all the possible attributes, the goal is to reduce the feature choices to a set with a small number of features that are as powerful, representable and general as possible. Feature engineering, including input representation, feature design, evaluation, and optimization, is essential to the success in machine learning. For unstructured data like images and texts, feature engineering can often become the bottleneck in learning related tasks. Selecting the most effective and descriptive features can improve performance, proficiency, and precision in quantification applications, or enhance a good classifier in classification. Features are domain-specific, therefore, in order to express input explicitly, automatically, fully, yet intuitively, substantial knowledge of the applications and the nature of the input is often required in deciding what features to use and optimizing the design. This thesis introduces a new set of feature engineering algorithms for medical research of 3D CT skull images in understanding craniosynostosis disorder. Our aim is to design effective low-dimensional features that can be used to classify the top three craniosynostosis disorder classes (sagittal, metopic and unilateral coronal), quantify shape-related deformity related to these three classes, and understand the effects of pre-post surgery change using our selected features as part of the full circle evaluation

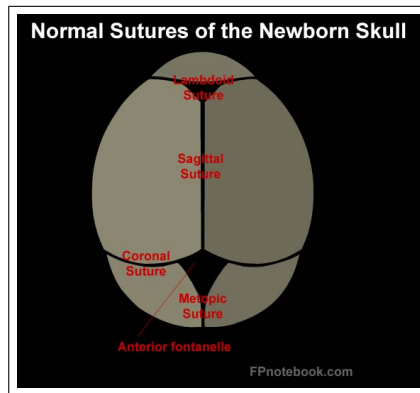


Figure 1.1: Top is the posterior and bottom is the anterior of a skull. Also shown are the four main sutures of the calvarial vault.

and optimization effort.

**Craniosynostosis** is a birth defect that occurs when one or more sutures, the fibrous joints of the skull, fuse prematurely. Despite the prevalence of this condition, the natural course of craniosynostosis is not well understood. During birth, the infant's head needs to pass through a narrow birth canal, but in the first three years after birth, an infant's skull needs to grow rapidly in response to a fast developing brain inside [5]. An infant's skull is made up of several bony plates (calvaria), connected by sutures. The persistence of sutures between the calvaria is necessary for skull malleability during birth and expansion of the cranial vault during brain growth. As shown in Fig. 1.1, the four main sutures of the calvarial vault are the sagittal suture, left and right coronal sutures, metopic suture, and left and right lambdoid sutures. The sutures must remain unossified so that the skull can stay malleable and the brain can have enough space to grow properly. Most craniosynostosis cases are isolated, with only one fibrous suture on an infant's skull fusing prematurely, but there are also syndromic cases with multiple affected sutures. A skull cannot easily expand perpendicular to a closed suture, which redirects growth parallel to the closed suture. Subsequently, a misshapen head and frequently abnormal facial features are induced [6].

Craniosynostosis occurs in one in 2,000 to 2,500 live births [5]. Sagittal synostosis, the most common form, represents about 40% to 55% of the non-syndromic cases. Coronal synostosis, the second most common synostosis, represents about 20% to 25%. Metopic

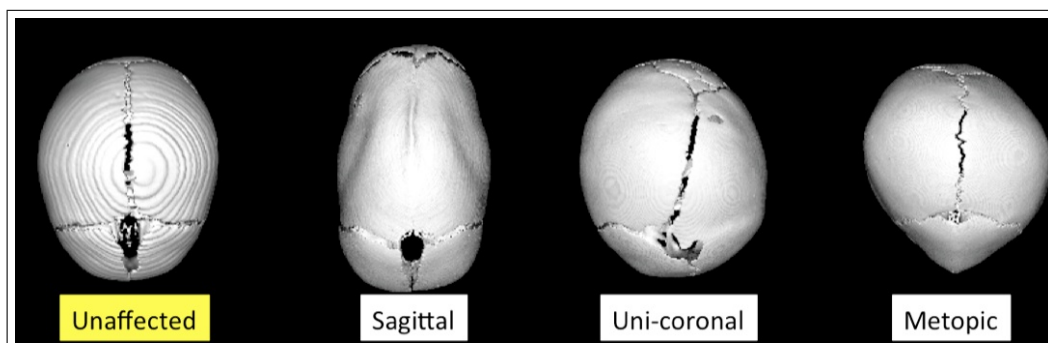


Figure 1.2: Shapes of unaffected (left), sagittal, uni-coronal and metopic synostosis skulls.

synostosis, the third most common synostosis, represents about 5% to 15%. Each class shape (sagittal, unilateral coronal and metopic) is illustrated in Fig. 1.2. If left untreated, craniosynostosis can be associated with increasing intracranial pressure and neurocognitive delays. For instance, a patient may suffer regular dizziness, visual impairment, sleep apnea, lower IQ or mental retardation [7] in addition to abnormal appearance.

Currently, the diagnosis of craniosynostosis relies on clinical evaluation by a trained clinician. During an infant's well-child visits to a pediatrician, the doctor regularly checks the growth of the infant's head while performing the physical examination. If synostosis is suspected, a CT scan of the head may be ordered as part of a standard diagnostic procedure. Sometimes the deformity caused by craniosynostosis may be mild at birth, and the signs can take a few months to become visually noticeable; however, early detection is essential to a timely surgery, while the infant is experiencing rapid brain growth. The objective of the surgery is to allow cranial expansion so that there will be adequate space for the brain to grow, intracranial pressure can be prevented and a normal appearance of the child's head can be restored. Although clinicians can easily diagnose craniosynostosis and classify its type, being able to quantify the condition (i.e., shape-deformity) automatically is important. Manual coding by expert reviewers is expensive, time-consuming, and probably unreliable without extensive pre-training. Automated platforms, once they are developed, are a fast, reliable and relatively inexpensive method for obtaining precise quantification of large data sets. Future clinical applications, in which for example a surgeon might want to quantify

pre- to post-surgery change, would be quite impractical using manual ratings in a clinical setting.

The goal of this work was to design, evaluate, learn and optimize features that are specific for shape-related craniosynostosis disorder studies, so that new quantification measures could be developed and tested on large numbers of CT subject images from multiple different sites.

## Chapter 2

### RELATED WORK

A literature review has shown that by applying feature design techniques to analyze 3D mesh data, we can overcome some of the long standing challenges in quantifying the shape-related deformity caused by craniofacial disorders. We first discuss related work in analysis of craniosynostosis disease.

#### **2.1 Local, curvature discrepancy from normality and fusion index**

To classify craniosynostosis skulls, Mendoza *et al.* [8] introduced a statistical shape model. Local regional malformations, segmented by cranial bones and ridging of sutures, were characterized into quantitative descriptors. The 71 features from each synostosis skull were computational, geometrical measures of suture fusion index, local dense deformation, and local curvature discrepancy in comparison to the most similar available normal shape in the training set. This feature design required projecting the surface model into the principal component analysis (PCA) shape space. Landmark points were marked by hand and then, were used only to locate the base plane and extract the region of interest. In addition to the nasion and opisthion anatomical landmarks, Mendoza used left and right dorsum sellae landmarks as well. After locating the base plane, the method was completely landmark free. When analyzing each synostosis skull, the approach heavily depended on correctly selecting the most similar unaffected skull from the control class to personalize and compute the malformations and curvature discrepancies. Mendoza was able to do so because of the ratio between his relatively high number of unaffected skull images and low individual affected ones. There were 90 normal subjects but 27 sagittal, 16 metopic, 3 right unilateral coronal, and 5 left unilateral coronal skull images in his experiment. The diagnostic features could be categorized into three: 1) fusion index to separate open from close sutures, 2) local estimate to compute the Euclidean distance between every single point in a synostosis



surface to the closest point in its normal shape reference surface model, and 3) absolute local curvature discrepancy in comparison to the normal shape reference surface model. Both local deformations and curvature discrepancies were measured in millimeters in respect to the normal shape reference. From each subject, a fusion index, deformation and curvature discrepancy averages were obtained across all six suture regions and five cranial bones. The accuracy of classification resulted in 95.7%, sensitivity 92.7%, and specificity 98.9%.

## **2.2 Feature-invariant image registration**

To quantify head growth, indirect intracranial volume change, and overall surgical outcomes, de Oliveira *et al.* [9] presented a semiautomatic, landmark free, rigid image registration-based analysis method. He aimed for landmark free approach because extensive cranioplasty after surgery could cause anatomical landmarks in the cranium to relocate unpredictably. Each post-surgery image was aligned and transformed iteratively, then registered basing on its static invariant pre-surgery features in the maxillofacial, an area that was not affected in the surgical intervention and could preserve major characteristics between pre- and post surgery images. As a result, both the source and the target meshes could be used to compute a minimum Euclidean distance matrix between the two in order to allow assessing their morphological differences. The method also showed the two aligned and overlaid meshes visually in order to illustrate the morphological changes in the three-dimensional space. The experiment reported local deformations ranging from 0 to 21 mm, mean minimum distance at 0.58 mm, and maximum of the minimum distances at less than 2.0 mm between the pre-surgery and 9 days after the surgery; whereas between the 9 days after the surgery and 1-year after the surgery, local deformations ranged from 0 to 19mm, mean minimum distance was 1.63 mm, and maximum of the minimum distances was less than 3.0 mm.

## **2.3 Three-dimensional vector analysis**

To characterize skull morphology for applications in image diagnosis, surgical planning and outcome assessment, Marcus *et al.* [10] demonstrated and statistically validated a three-dimensional cranial surface point cloud based vector analysis method. This highly interactive application was written in Matlab, required an user to enter forsum sella, na-

sion, and vertex landmark positions and a specific degree interval manually to produce a 3D surface point sphere cloud starting from the dorsum sella origin. Then, tabular vectors of the azimuth, elevation, and magnitude were computed. Finally, inter marker distances, their averages between each of the marker pairs, and 437 cranial surface points were calculated, then averaged and analyzed as single descriptive statistic value. Both the mean standard deviation and the mean standard error resulted in less than 0.5mm, with a mean of 0.52% of the inter marker measurement in comparing this method with a baseline CT-based measurement.

#### **2.4 Symbolic signatures**

Ruiz-Correa *et al.* [11] developed the cranial image, a high-dimensional distance matrix representation of the skull, and used it to classify different types of craniosynostosis. Lin *et al.* [12] extended the methodology to symbolic-signature descriptors derived from the cranial image. With the symbolic descriptors capturing the information in the much larger cranial image, Lin obtained a more compact representation of a 3D shape. The symbolic shape descriptors encode global geometric properties that capture the uniqueness of each shape class by probabilistic modeling of their local geometric properties.

#### **2.5 Azimuth-elevation-angle histogram**

Atmosukarto *et al.* [13] determined several measures for quantifying the severity of deformational plagiocephaly (DP), a postnatal flattening of the back of the skull. Her descriptors used the concept of an azimuth-elevation-angle histogram of the surface normals of the back of the head and produced severity errors that were functions of the left and right side bins of these histograms. Atmosukarto's approach achieved high accuracy (all classification were greater than 90%) in distinguishing DP cases from non-DP controls. Her *asymmetry score* descriptor provided the best overall discrimination.

#### **2.6 Euclidian distance matrix**

Lele and Richtsmeier [14] have used descriptors that combined *Euclidian distance matrix analysis* (EDMA) and likelihood-based classification methods but the approach led to a

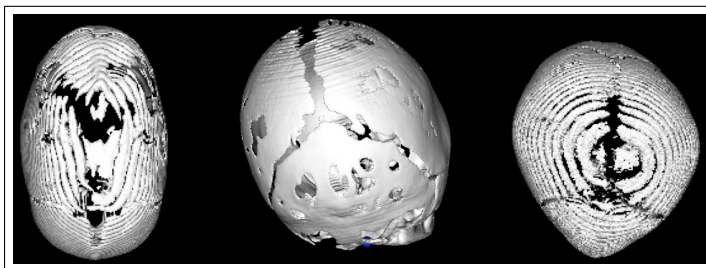


Figure 2.1: Imperfections like holes, rings and noise as seen on some older CT scans can make processing and shape analysis difficult.

high error rate in the 18 – 32% range, as discussed in Ruiz-Correa [15].

## 2.7 Sparse logistic regression models

Yang et al. [4] developed a plane-based retrieval system that produced a variation of Ruiz-Correa’s cranial image. To classify, Yang used logistic regression,  $L_1$ -regularized logistic regression, the fused lasso and the clustering lasso classifiers but the method requires a high-dimensional  $100 \times 100$  distance matrix to achieve mid-90% classification accuracy. Yang traded higher computational and memory costs for better performance. Her method was also sensitive to poor resolution, noise or other imperfections on the original CT scans, as shown in Fig. 2.1; consequently, only 70 skull images could be used.

Our work builds on the work of Yang, but there are important differences. Our methods were able to process additional data including 149 total skull images of four different types: sagittal, unilateral coronal, metopic, and control. Yang had less data and no control images. Yang’s features were simply a set of points taken along the contour of the skull on multiple different planes. We have developed specific shape descriptors for our work. Finally, because Yang had no controls, her experiments could only classify abnormal compared to other abnormal. We are able to classify abnormal compared to control, which is the more medically relevant task when it is used for diagnosis, as well as to compare our work to Yang’s by making the same two-class comparisons and multi-class comparisons she made.

## **2.8 *Classifying by visual inspection***

In some clinics, visual inspection, a labor intensive, manual process in designing, selecting, learning, optimizing, and utilizing features, was highly encouraged. For example, in Massimis clinics [10], CT scans were restricted to severe bone constriction and hypertrophic scalp veins or evident sellar deformation of the cranial vault. However, visual inspection is subjective and may be biased and limiting. Since procedures and test results that are consistent, efficient and reproducible are highly valued, developing an automated, 3D image-processing-based system for the characterization of craniosynostosis remains a research objective.

Even though our research was limited to the study of 3D CT skull images for craniosynostosis disorder applications, feature engineering can benefit many image analysis tasks in the discipline of computer vision for the medical applications or beyond. We next discuss related work in analysis of another craniofacial disease: autism spectrum disorders (ASD).

## **2.9 *Euclidean distance matrix analysis of facial morphology***

Using 3dMD images from 64 boys with ASD and 41 unrelated control boys, Aldridge applied Euclidean Distance Matrix Analysis (EDMA) to identify unique facial features of an affected ASD boy population [16]. All 105 boys were between 8 and 12 years old. EDMA is a linear distance-based morphometric approach. It does not require any registration or fitting criteria. In Aldridge’s work, the 17 anatomical landmarks were manually annotated on each mesh [16] and from these 17 facial landmarks, Euclidean distances were computed. Aldridge concluded that boys with ASD demonstrated differences in facial morphology compared to unaffected control boys [16]. In Aldridge’s EDMA, 39 out of 136 total measured distances were statistically significantly different between the affected and unaffected population groups. For instance, distance from glabella to inner canthi on the ASD group is significantly shorter, as are the distances also shorter from nasion to inner canthi, from nasion to nose, and from nasion to philtrum. By contrast, the distance from mouth to inferior nasal region on the ASD group is significantly longer, as is the distance longer from inner and outer canthi to the lateral upper face [16]. Aldridge’s work analyzed the shape of the mid face; whereas our work focused on the shape of the skull.

### **2.10 Landmark-based adapted geometric morphometrics**

Geometric morphometrics (GM) is a commonly used landmark-based statistical analysis of shape and size [17]. One of its primary benefits is to reveal the shape variation or the degree of shape differences between two or more objects. GM relies on the use of landmarks, which are often manually identified and placed on each individual image by an expert. The Procrustes method is the gold standard for obtaining the shape information from each image by first aligning its landmarks [1] [2]. However, the need for precise landmarks poses several challenges. First, placing landmarks manually on an image is both time-consuming and error-prone. Second, finding landmarks on all groups of interest could be difficult or impossible. Third, identifying more landmark points is always desirable, but the task can be unrealistic to reach. To overcome these types of landmarking problems, thin-plate spline interpolation can be applied to assign semi-landmarks on curving outlines of an image. By extending the morphometrics techniques to include both Procrustes transformation and thin-plate spline interpolation methods, we can profile and quantitatively identify various shape characteristics from an image [3] [17]. In Procrustes analysis, landmarks in each group, including its averaged landmarks, have the same relative locations [3]. Relative location allows an implied correspondence to be specified among a participating set of shapes [3]. The thin-plate spline technique aligns two landmark sets while the areas in between landmark points are smoothly interpolated [3]. The thin-plate spline algorithm can also be used to unwarped an image. Thus, it is a deformation tool that can be used to describe shape differences in a 3D surface image [3]. With this tool, an abnormal shape can be distinguished by comparing it against an averaged normal shape in the same category (*i.e.*, gender, age, race, and so forth).

To analyze face shape in his thesis [18], Hutton applied adapted geometric morphometrics to produce high-dimensional features filled with tens of thousands of dense correspondence vertices. He implemented the dense surface model algorithm, which, unlike other approaches, required only the landmarks but no other pre-processing. Hutton's algorithm was able to automate the production of the full dense correspondence between the surfaces, directly from the acquired 3D surface meshes. Adapted GM methods have also been ap-

plied to study craniofacial shape in [3] [19] [20]. Unlike traditional geometric morphometrics approach, which places landmarks across each face surface, Hutton’s method optimized the usage of tens of thousands of points typically already available on a face scan. As shown in Hutton’s thesis, these greatly increased extra data were proved to improve the accuracy and efficiency of classification tasks and in data modeling as well.

### ***2.11 Dense surface-modeling of facial morphology***

Using 3dMD images from 72 boys with ASD, 128 first-degree relatives of the boys with ASD, and 254 unrelated control boys, Hammond applied both adapted geometric morphometrics and Dense Surface-Modeling (DSM) techniques to identify some unique facial features of an affected ASD population [19]. Hammond’s DSM techniques are similar to the adapted geometric morphometrics above in including both Procrustes transformation and thin-plate spline interpolation. To differentiate an ASD face, a principal component analysis (PCA) was used to compare each target dense corresponding surface mesh to an averaged face representation (i.e., an averaged group representation of an unaffected control boy population). In Hammond’s work, the 18 anatomical landmarks were manually annotated on each mesh [19]. Because the differences between an ASD face and a control face are subtle, he tried several experiments: 1) analyzing only regions where landmarks could be placed, 2) increasing the number of landmarks, 3) employing the Euclidean distance between the DSM-based mesh of an individual face and its mirrored form as an index of symmetrical measure. Hammond concluded that boys with ASD show statistically significant facial asymmetry, particularly near the supraorbital region, zygomatic arch and forehead. On one hand, unaffected mothers of boys with ASD also display similar significant facial asymmetry. On the other hand, neither unaffected fathers of boys with ASD nor unaffected siblings of boys with ASD show statistically significant facial asymmetry [19].

## Chapter 3

### APPROACH AND METHODOLOGY

As shown in Fig. 3.1, our system is a general platform for 3D craniofacial shape analysis. There are five modules:

1. Data Acquisition and Preprocessing
2. 3D Mesh Region of Interest Extraction and Re-orientation
3. 2D External Contour Points Extraction from each 3D Mesh
4. Aggregate and Low Level Features Extraction
5. Classification and Analysis

#### ***3.1 Data acquisition and preprocessing***

There are five steps in the procedures for data acquisition and preprocessing including 1) CT acquisition, 2) CT cleaning, 3) mesh extraction, 4) mesh normalization, and 5) landmarking.

**CT acquisition** For our craniosynostosis study, the 3D computed tomography (CT) scans of heads were collected from hospitals in four different cities: Atlanta, Chicago, Seattle and St. Louis. Each CT image has 64 slices and each slice is stored in 16-bit and 500 x 500 pixel resolution according to the Digital Imaging and Communications in Medicine (DICOM) standard.

Our study is limited to three types of synostosis: sagittal (the affected suture is between the parietal bones), metopic (the affected suture is between the frontal bones) and unilateral coronal (the affected suture is between the frontal and the parietal bones on either the right side or the left side of the skull). For the control dataset, the Radiology database at Seattle

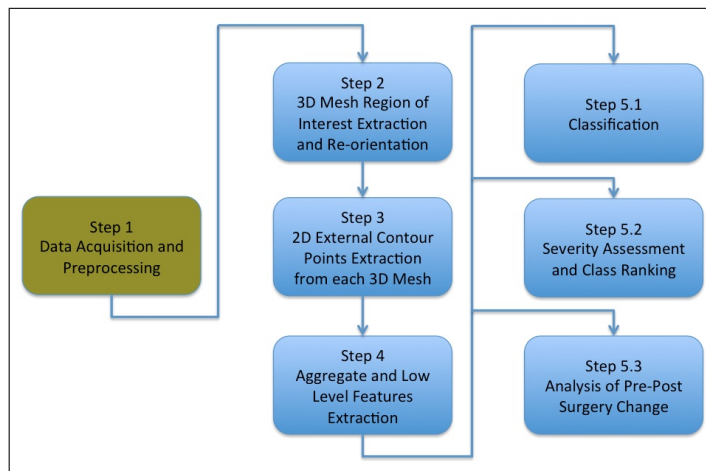


Figure 3.1: Flow chart of our system. Step A *Data Acquisition and Preprocessing* is not part of the automated system being developed.

Children’s Hospital was interrogated for children that had head CTs at age 2 years and younger. First, all children with craniofacial malformations, including craniosynostosis, were excluded. Next, CT scans obtained for minor head trauma, headache, or other reasons that would not effect calvarial shape were reviewed in 3D format. Finally, cases without abnormalities in calvarial form were used as controls. For our experiments, 149 skull meshes were included. 34 images were from the unaffected subjects (children who do not have craniosynostosis disorder), and 115 images were from the affected subjects (children with sagittal synostosis, unilateral coronal synostosis, or metopic synostosis). All the subjects were under two years of age.

**CT cleaning** Each CT image is cleaned so that all surfaces below the chin (e.g. the neck, shoulder, clothing or hands) are deleted. We do not repair the surface, fill holes or apply any smoothing algorithm to the cleaned CT image.

**Mesh extraction** From the CT volume data of the head, our system first extracts the skull slices and creates a single 3D image of the skull surface mesh. Each mesh contains between 140,000 and 850,000 vertices. If needed, we clean up the mesh (i.e, by removing any trace of the neck bone) to ensure best possible normalization and landmarking.



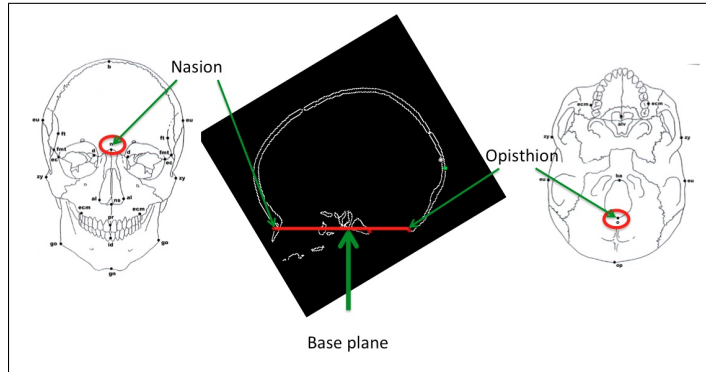


Figure 3.2: Identifying the base plane based on the nasion and opisthion anatomical landmark points. This base plane was used as one x-y-z coordinate plane to re-orient the entire extracted 3D ROI.

**Mesh normalization** Because our 3D CT scans are of random pose, our system next performs normalization on the cleaned skull surface mesh to ensure the skull poses are symmetrical between its left and right sides. For our analysis and classification, it is also important that all skull surface meshes use the same coordinate reference. Therefore, after the normalization, the skull should face front and center, and is ready for the landmarking step.

**Landmarking** The final step in this module is landmarking, which locates and records the x-y-z locations of two landmark points: nasion and opisthion. We use only two landmark points to define our base plane. To assure consistency, the open source application meshlab is used to mark these two points by hand on each 3D surface mesh. The x-y-z location values of these two points are then stored in a text file so that the points can be used to extract the ROI and contour points for data analysis and classification.

### ***3.2 3D mesh region of interest extraction and re-orientation***

Based on the location of the nasion and opisthion landmark points, the algorithm identifies a base plane as shown in Fig. 3.2. The surface mesh on and above this base plane is considered to be the region of interest (ROI), which our algorithm extracts and uses for the remaining analysis. This tilted base plane replaces one of the three x-y-z coordinate planes

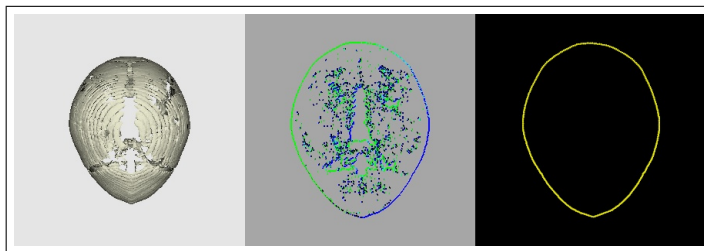


Figure 3.3: Extracting a 2D external contour (right) by first projecting the 3D surface mesh (left) onto a 2D plane (middle). Keeping only the exterior points from the silhouette. This approach allows processing and shape analysis to be done even on older CT scans that have noise and challenging imperfections.

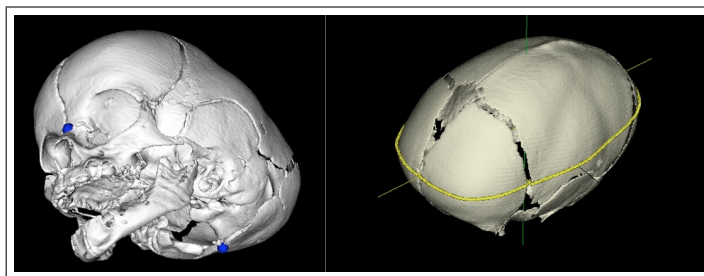


Figure 3.4: Original image with both nasion and opisthion anatomical landmark points in blue (left). Removing all vertices below the base plane to obtain the extracted ROI (right). The contour (yellow line on right) is rescaled and translated so that it shares the same center and bounds as the ROI.

(in our case, the new z-plane). Subsequently, the coordinate reference of the 3D ROI is re-oriented. This module standardizes and positions the extracted ROI uniformly to ensure accurate comparison and later analysis.

### ***3.3 2D external contour point extraction from each 3D mesh***

The bird's-eye view from the top of a skull can reveal many unique characteristics for describing its shape. Our shape analytic system uses a simple 3D projection-based contouring technique to extract exterior shape information from the 3D surface mesh as a whole. Our contour extraction module first projects a top view of the 3D ROI onto a 2D plane. Then it extracts only the exterior contour points uniformly in one-degree steps for a 360-degree

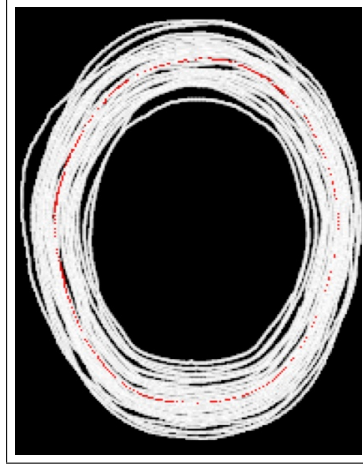


Figure 3.5: By using the Procrustes method [1] [2] [3], a mean (or average) contour is computed from our 34 unaffected skull dataset. Each white line represents a contour of an unaffected skull in the 34 dataset; whereas the red line represents the averaged contour of the entire unaffected group. This red line is identical to the green lines in Fig. 3.6

sweep. The top view of a 3D extracted ROI and its 2D external contour are shown in Fig. 3.3. The contour is rescaled and translated so that it shares the same center and bounds as the extracted ROI, as shown in Fig. 3.4. Different numbers of contour points were experimented with by varying the degree interval, but no significant differences were observed in their resulting classification performance.

### 3.4 Aggregate and low-level feature extraction

Let the 2D contour be defined with an x-y axis, whose origin is at the center of the shape. Let  $P = (p_1, p_2, \dots, p_{360})$  be the  $N = 360$  contour points used to generate the features.

Our system uses two kinds of features: 1) low-level features that are computed directly from the contour points and 2) aggregate features that combine multiple low-level features mathematically to produce a single score value.

*Compare to Mean Unaffected* (cmp2Mean) is a single value descriptor, which compares the contour to the contour of the mean (or average) in the unaffected subject group. As shown in Fig. 3.5, the mean contour points are computed based on the contour points from all unaffected subjects. The mean contour was extracted by using Procrustes transfor-

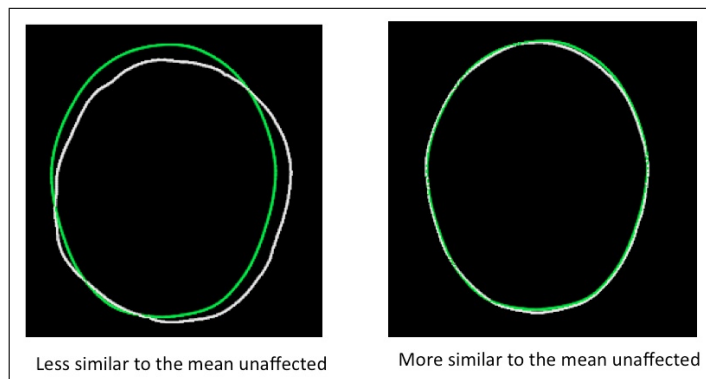


Figure 3.6: (right) A more mean-unaffected like skull and (left) a less mean-unaffected like skull. The green lines on both images are identical. The green line represents the mean contour of the entire unaffected class contour. The white lines on both figures represent two contours from two different skulls.

mation. The Procrustes method is the gold standard for obtaining the shape information from each image by first aligning its landmarks, or contour points [1] [2]. In Procrustes analysis, landmarks in each group, including its averaged landmarks, have the same relative locations [3]. Relative location allows an implied correspondence to be specified among a participating set of shapes [3]. Thus, it is a deformation tool that can be used to describe shape differences in a 3D surface image [3]. With this tool, an abnormal shape can be distinguished by comparing it against an averaged normal shape in the same category. A higher error score value (in comparison to the mean unaffected) indicates a higher dissimilarity of this skull to the mean representation of the unaffected group. The skull on the right in Fig. 3.6 resembles more like the mean unaffected. This aggregate descriptor is not used in classification module.

*Width to Length Ratio* ( $w2l$ ) describes the ratio of the width to the length of a skull. This is the simplest and perhaps the most widely used craniofacial feature, though not the most powerful in this experiment. A narrow and elongated skull shape has a lower *width to length ratio* value; whereas a round skull shape has value close to 1.0.

*Compare to Circle* ( $cmp2Circle$ ) is a single-valued descriptor, which compares the 2D contour to the shape of a circle. A higher error score value indicates a less circular skull, as illustrated in the left of Fig. 3.7. A more circular skull is shown in the right of Fig. 3.7.

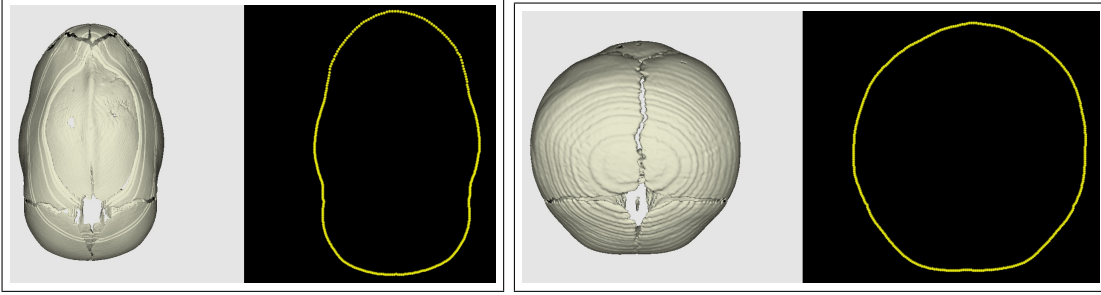


Figure 3.7: (left) A less circular skull; (right) a more circular skull.

In order to avoid errors induced by skull size in this aggregate measure, size normalization is used. Otherwise, a CT scan that was acquired from an older child, whose skull might be larger would be incorrectly scored with a higher error value.

Let  $r_{max}$  be the maximum distance from origin to a point  $p \in P$  and  $r_{min}$  be the minimum distance. The average distance  $r_{avg}$  is used to construct a circle centered at the origin. Then, the normalized feature *cmp2Circle* is defined by (3.1)

$$cmp2Circle = \frac{\sum_{p \in P} \|p_{dist} - r_{avg}\|^2}{N \times r_{avg}}. \quad (3.1)$$

*Symmetry* is a single-valued descriptor, which compares the contour points of the left and right sides to determine the symmetry of a skull. A higher error score value indicates a more asymmetrical skull. As shown in Fig. 3.8, our algorithm divides the contour into left and right sides. The yellow lines represent the complete contour extracted from both sides of a skull. The white lines are the mirror image from one side, flipped to the opposite side so that the symmetrical characteristic of a skull can be easily visualized. If the yellow and white lines meet exactly, the skull is perfectly symmetrical. For example, the unilateral coronal skull on the right side in Fig. 3.8 shows a highly asymmetrical characteristic. The side where the white line lies is the side our algorithm determines to have an affected suture.

Let  $P_R = (pr_1, pr_2, \dots, pr_n, \dots, pr_{180})$  be the 180 points on the right side of the contour,  $P_L = (pl_1, pl_2, \dots, pl_n, \dots, pl_{180})$  be those on the corresponding left side.

Let  $pr_n = (x, y)$  and its corresponding point  $pl_n = (a, b)$ . Let  $pl'_n$  be the mirror image of  $pl_n$  along the y-axis. With origin at  $(0, 0)$ ,  $pl'_n = (-a, b)$ . The Euclidean distance

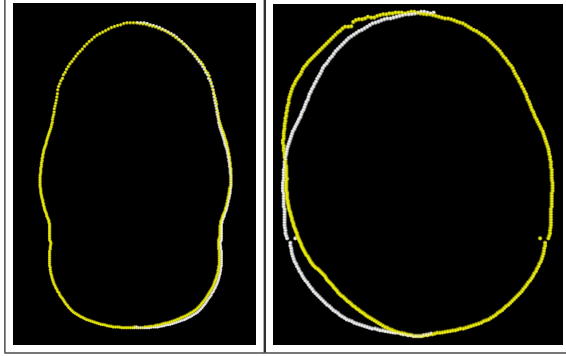


Figure 3.8: Illustration of a symmetrical sagittal synostosis skull (left) and an asymmetrical unilateral coronal synostosis skull (right).

$d(pr_n, pl'_n) = \sqrt{(x+a)^2 + (y-b)^2}$ . Then, the normalized feature *symmetry* is defined by (3.2)

$$symmetry = \frac{\sum_{pr \in P_R, pl \in P_L} d(pr, pl')}{N \times r_{avg}}. \quad (3.2)$$

*Angle* is a low-level vector descriptor, which describes the angle between a line with the slope of two neighboring contour points and the horizontal x-axis. In our experiments, there are 360 contour points. Therefore, there are 180 angle descriptor features on the front side of the skull contour, and there are another 180 on the back.

This feature is a 360-dimensional vector whose values are computed at each pair of consecutive contour points. For such a pair  $(p_i, p_j)$ , the angle is given by the arctangent as in (3.3)

$$angle = \arctan\left(\frac{y_j - y_i}{x_j - x_i}\right) \times \frac{180^\circ}{\pi}. \quad (3.3)$$

*Radius Distance* is a low-level vector descriptor, which describes the radius distance from each contour point to the center of the extracted surface mesh. There are a total of 360 contour points, one degree apart. Therefore, there are a total of 180 radius distance descriptor features on the front side of the skull contour, and there are another 180 on the back.

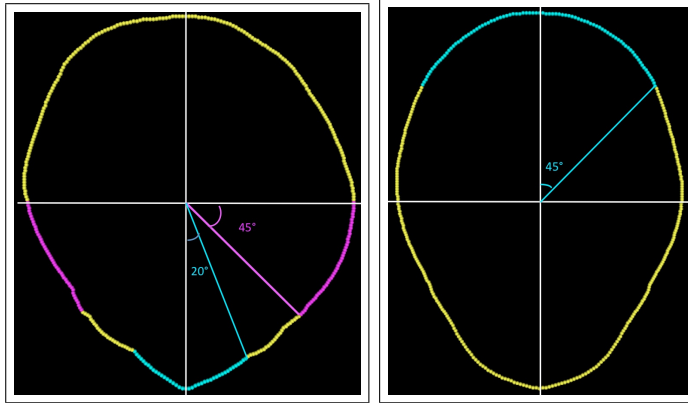


Figure 3.9: (left) Left and right front-center contours, which fan 45 degree from the horizontal x-axis, are shown in magenta. Left and right front-tip contours, which fan 20 degree from the vertical front y-axis, are shown in cyan; (right) left and right back contours, which fan 45 degree from the vertical back y-axis, are shown in cyan.

This feature is a 360-dimensional vector whose values are computed at each contour point. For a point  $p_i$ , the distance is given by its distance to the origin  $(0, 0)$  as in (3.4)

$$\text{dist}(p_i) = \|p_i\|^2. \quad (3.4)$$

The next two features are derived from the feature Angle. The Angle feature gave rise to two mean quantitative scoring scalar values, *Average Slope Angle of Front Tip* and *Average Slope of Back*.

*Average Slope Angle of Front Tip* (front) and *Average Slope Angle of Front Center* are the two averages of the *Angle* vectors describing the left and right front tip angles (shown in cyan on the left of Fig. 3.9) and left and right front center angles (shown in magenta on the left of Fig. 3.9) on a skull. *Average Slope Angle of Back* (back) is the average of the *Angle* vector describing the left and right back angles (shown in cyan on the right of Fig. 3.9) on a skull. For a more deformed metopic skull (shown in Fig. 3.10), the sharpness of its front tip angles remain high towards the tip; whereas, in a less deformed metopic skull (shown in Fig. 3.11), the sharpness of the front angles reduces towards the tip. For a more deformed sagittal skull (shown on the left of Fig. 3.12), the back feature scoring value tends to be higher than on a less deformed sagittal skull (shown on the right of Fig. 3.12).

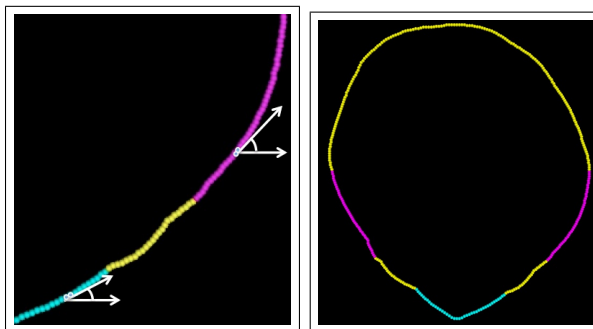


Figure 3.10: (left) Components of the Angle vector at two different segment points along a contour: front-center segment contour in magenta and front-tip segment contour in cyan; (right) *change of average slope angle towards front tip* (COA) of this more deformed metopic skull is 27.38 degree.

*Change of Average Slope Angle Towards Front Tip* (COA) describes the angular difference between the average angle of the front-center contours and the front-tip contours (the two averages are illustrated on the left of Fig. 3.10 and on the left of Fig. 3.11). For a more deformed metopic skull (shown in Fig. 3.10), its average front-center angle tends to be lower and its average front-tip angle tends to be higher in comparison to the two averages in a less deformed metopic skull. As a result, the angular difference, COA is smaller in a more deformed metopic skull than in a less deformed metopic skull (shown in Fig. 3.11).

### 3.5 Tasks

Our platform can support three different kinds of tasks: classifications, severity assessment and class ranking, and analysis of pre-post surgery change.

#### 3.5.1 Classification

In the *classification* module, sequential minimal optimization (SMO) and logistic regression, both of which are linear classifiers that assign a score to predict class are used from the WEKA suite of classifiers. The SMO classifier is essentially a support vector machine. In general, 10-fold cross-validation experiments are applied to evaluate the performance of the trained classifiers, except when comparing to previous results that used 3-fold cross-



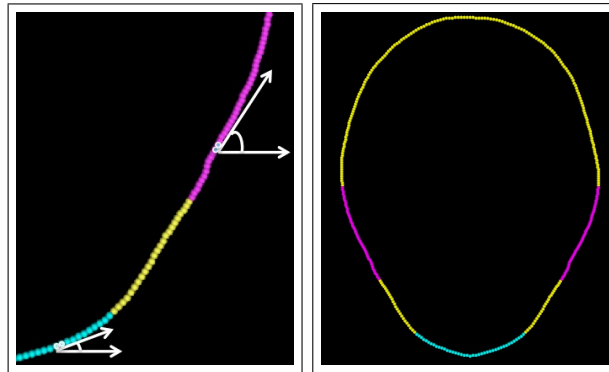


Figure 3.11: (left) Components of the Angle vector at two different segment points along a contour: front-center segment contour in magenta and front-tip segment contour in cyan; (right) *change of average slope angle towards front tip (COA)* of this less deformed metopic skull is 40.93 degree.

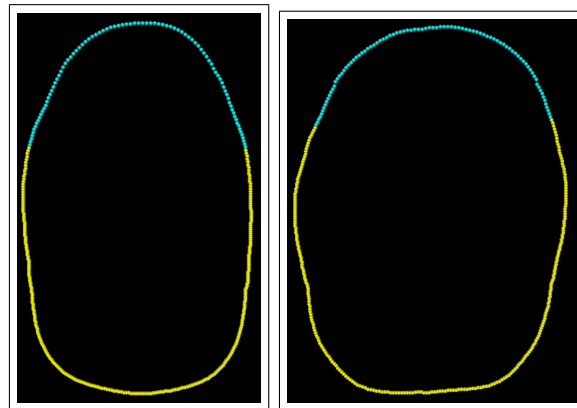


Figure 3.12: The more deformed a sagittal skull is, the more angular its back angles are. (left) this more deformed sagittal skull has *average slope angle of back* at 56.959 degree; (right) this less deformed sagittal skull has *average slope angle of back* at 42.291 degree.

validation. Each experiment is run several times by randomizing the incidents in order to observe any unexpected outliers, unusual patterns or unexplainable randomness in the results. Prediction accuracy is recorded.

### 3.5.2 *Severity Assessment and Class Ranking*

In the classification module, a general platform, upon which basic shape measures, both single-valued and vector-valued were extracted from a single plane projection of the 3D skull, was developed. This technique allowed images, that would otherwise be eliminated due to poor resolution or noise on their original CT scans and to distinguish with high accuracy between abnormal cases in each class and controls, to be processed. In *severity assessment and class ranking* of pre-surgery images, features were re-engineered and expanded so that the updated versions can be used to score all the images uniformly, expressively and completely. From each class, the features, that have above or close to 0.5 correlation to the ranking orders provided by the two human experts, were selected. Based on each individual feature score of these selected feature list, an unique ranking order was automatically generated so that all the skulls in each class was sorted according to this particular feature score, which is one interpretation in describing the deformity.

### 3.5.3 *Analysis of Pre-Post Surgery Change*

In *analysis of pre-post surgery change effect* module, the same selected features that were used in the severity assessment and class ranking module were used here to compute the scores for the post-surgery skulls so that the post-surgery skulls can be quantitatively compared to their pre-surgery counterparts. For completeness, the same selected features were also used to generate the scores for the unaffected skulls so that the post-surgery skulls can be measured against the full range of the unaffected class. For each synostosis class, we want to understand not just what changes have taken place after the surgery but also quantitatively how much change have occurred, and how change effects vary from one synostosis class to the other.

## Chapter 4

**CLASSIFICATION EXPERIMENTS AND RESULTS**

In our classification experiments, there were three affected skull datasets: a 57 subject sagittal dataset, a 33 subject uni-coronal dataset, and a 25 subject metopic dataset.

**4.1 Classify abnormal as compared to controls**

Each affected skull dataset was run against the same 34 unaffected skull dataset. To compare the effectiveness in distinguishing each affected group from controls, the above-described features were tested, both individually and in combination.

Table 4.1 gives the results of trying each of the four features individually. Column 1 shows the accuracy for the single-valued Compare to Circle (cmp2Circle) feature. Column 2 shows the accuracy for the single-valued Symmetry (symmetry) feature. Column 3 shows the results for the Angle feature (angleFnB) taken from 360 positions on the front and the back of the skull. Column 4 gives the accuracy for the Radius Distance feature (distFnB) taken from 360 positions on the front and the back of the skull. In both tables, #features refers to the total number of aggregate and low-level features used in that column.

Table 4.1: Accuracy with standard deviation of using each descriptor (column) individually to distinguish each affected skull dataset (row) from 34 unaffected skulls.

	cmp2Circle	symmetry	angleFnB	distFnB
#features	1	1	360	360
Sagittal	94.50 (4.46)	67.54 (5.05)	97.22 (3.93)	95.06 (4.79)
Uni-coronal	73.08 (10.28)	91.15 (5.72)	89.56 (9.28)	86.65 (7.57)
Metopic	57.58 (1.60)	57.58 (1.60)	99.17 (2.64)	91.59 (8.79)

In Table 4.2, column 1, (c-s) contains accuracy results using both comp2Circle and symmetry. Column 2 shows accuracy for the combination of these two features plus all the angle features (c-s + angleFnB). Column 3 contains the accuracy for the first two features plus all the distance features (c-s + distFnB). Column 4 shows the accuracy for all of the features (all). The total of all features is 722.

Table 4.2: Accuracy with standard deviation of using each descriptor (column) collectively to distinguish each affected skull dataset (row) from 34 unaffected skulls.

	c-s	c-s + angleFnB	c-s + distFnB	all
#features	2	362	362	722
Sagittal	96.70 (3.87)	97.22 (3.93)	95.61 (4.29)	95.58 (4.38)
Uni-coronal	88.74 (6.58)	91.04 (7.54)	92.58 (5.99)	89.51 (10.13)
Metopic	57.58 (1.60)	99.17 (2.64)	91.59 (8.79)	99.17 (2.64)

#### ***4.2 Classify two and multi-abnormal as compared to each other***

In Table 4.3, an additional experiment was performed in order to compare with Yang’s results. Here, 3-fold cross validation with classifiers SMO and logistic regression were used in order to perform a direct comparison. The results demonstrated that the descriptor comp2Circle is highly effective for sagittal detection, symmetry for uni-coronal, and angleFnB for most cases. Overall, the accuracy observed was higher in this system than in Yang’s, particularly when all the descriptors were used together.

Table 4.3: Accuracy of comparison to previous results [4]. C is coronal. M is metopic. S is sagittal.

		C vs M	M vs S	S vs C	Three-Classes
Yang	C lasso	95.71	95.71	94.29	92.86
	F lasso	94.29	94.29	95.71	81.43
	L <sub>1</sub>	92.86	95	93.57	91.43
	Log	86.43	86.43	76.07	90
all	SMO	99.67	99.64	98.89	99.2
	Log	96.55	96.34	100	-
angleFnB	SMO	100	100	100	100
	Log	98.28	96.34	100	97.39
distFnB	SMO	93.1	98.78	98.89	94.78
	Log	82.76	96.34	97.78	94.78
symmetry	SMO	87.93	69.51	93.33	73.04
	Log	91.38	70.73	93.33	73.91
cmp2Circle	SMO	81.03	93.9	100	82.61
	Log	79.31	93.9	100	86.96

### 4.3 Discussion

Classification was carried out to improve on prior work in which 1) no control data was available, 2) poor resolution, noise, missing slices, and other imperfections in the CT data

eliminated many scans from use, and 3) the quantification measure was based on the mathematics of the classification method, not on an intuitive measure of shape. This work has a control set, is able to solve the imperfect data problem for many CT scans, and provides both a simple projection technique and several intuitive shape measures as part of a general platform.

By applying this framework on a CT surface mesh, our system can distinguish affected skulls from unaffected ones. As shown in Table 4.2, the two single-valued features (cmp2Circle and symmetry) plus the vector feature of 360 angles (angleFnB) achieves accuracies of 97.22%, 91.04% and 99.17% on the classification tasks of sagittal, unilateral coronal, and metopic vs control, respectively. Furthermore, as shown in Table 4.3, when all features are used, accuracies reach 99.67%, 99.64%, 98.89% and 99.2% in four cases, respectively. These results show clear improvement over previous work [4].

Note that the angle descriptor (angleFnB) gave very high accuracies both in our own experiments of affected vs. control and on the comparison experiments with Yang’s work, which had no controls and included classifications of pairs of classes and a 3-way class comparison. The accuracy of this feature in the latter comparisons with the SMO classifier was particularly high, 100% in all four cases. Since we are using cross-validation, we do not suspect overtraining. Instead, we believe that this is just a much easier task than distinguishing affected skulls from controls. The three abnormal classes are very different from one another. The SMO is a very powerful classifier, and it was able to learn to fully separate these classes on the amount of data we possess. On the more difficult task of distinguishing affected from controls, above 99% accuracy was only achieved on the metopic vs. control task and required the angleFnB feature.

We also note that the cmp2Circle descriptor gave very high accuracies to cases that involved sagittal synostosis on our own experiments of sagittal vs. control and on the comparison experiments with previous work. Similarly, the symmetry descriptor gave very high accuracies to cases that involved unilateral coronal synostosis on our own experiments of uni-coronal vs. control and on the comparison experiments with previous work. The *symmetry* descriptor can assess and determine which side of a unilateral coronal synostosis skull has the affected suture. In this experiment, the algorithm correctly predicted the

affected sides in 94% of the total uni-coronal synostosis cases.

Classification is not our final goal; it merely allows us to develop and judge shape features to be used for quantification. The results from our experiments are very promising not just for this classification experiment but in assessing the severity of a skull's deformation caused by craniosynostosis and measuring the change effects from corrective surgery.

## Chapter 5

### SEVERITY ASSESSMENT AND CLASS RANKING EXPERIMENTS AND RESULTS

The 115-subject pre-surgery dataset used in this study includes 57 sagittal, 33 left or right unilateral coronal, and 25 metopic skull images.

#### 5.1 *Clinician ranking orders*

Within each of these 3 synostosis categories, two medical doctors, Expert1 and Expert2, separately used an interactive application to examine the 3D images and rank them according to the degree of their shape-deformity from least deformed (Rank 1) to most (Rank N).

#### 5.2 *Correlations and ranking comparisons*

For all the images in each of the three synostosis classes, the features that were described in Section 3.4 were computed, followed by an analysis of the Spearman's correlation coefficients between these features and the ranking orders provided by the two experts. Features that achieved correlations close to or above 0.5 are shown for each of the classes in the following order: 1) metopic, 2) sagittal, and 3) uni-coronal. The ordering of the classes reflects the success of the automated methods in correlating with the expert opinions. Correlations between the two experts are also given and also are highest for metopic, next highest for sagittal, and quite low for uni-coronal.

##### 5.2.1 *metopic class*

As shown in Table 5.1, the metopic ranking orders from the two experts were highly correlated at 0.7723. Nevertheless, a machine generated feature, COA, correlated at 0.8019 to Expert1 and at 0.8592 to Expert2, the highest correlation we found. As demonstrated



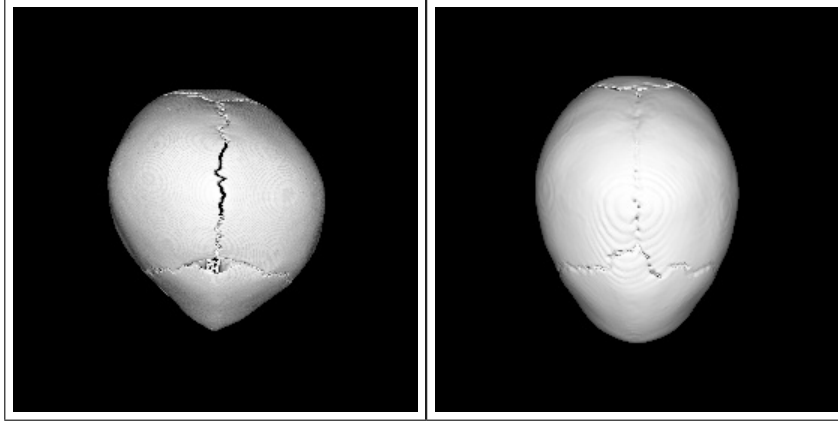


Figure 5.1: Illustration of a more shape-deformed metopic skull (left), which has less angular change at the front of a skull and a more persistent sharp angle towards the front tip, than a less shape-deformed metopic skull (right), whose contour gradually reduces in angular sharpness towards the front tip.

on the left of Fig. 5.1, the slope of the front contour changes less and remains sharp from the center towards the tip of the more deformed skull. Another feature, front, indicates the average angular slope sharpness of the front tip. Feature front was correlated at 0.7261 to Expert1 and at 0.7281 to Expert2.

	Expert1	Expert2	COA	front
Expert1	1	0.7723	0.8019	0.7261
Expert2	0.7723	1	0.8592	0.7287
COA	0.8019	0.8592	1	0.7411
front	0.7261	0.7287	0.7411	1

Table 5.1: Correlation coefficients of metopic ranking orders.

Fig. 5.2 and Fig. 5.3 show the top five most deformed and top five least deformed metopic class skulls in order of ranking by the COA feature and in comparison to the rankings of the front feature and those assigned by Expert1 and Expert2. Here, the four sets of ranking orders are reasonably consistent. However, the ranking of medium deformed skulls was less consistent, as ranking results show in Fig. 5.4. One way to explain this is to

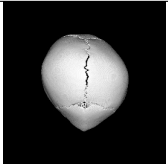
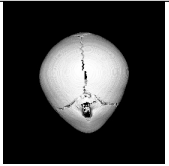
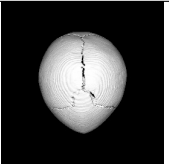
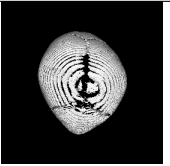
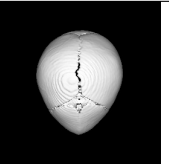
images					
COA	25 most	24	23	22	21
Expert1	24	21	10	20	23
Expert2	25	24	21	23	22
front	25	13	15	18	23

Figure 5.2: The 5 most shape-deformed of the total 25 metopic skulls. The 25th was the most severe skull and 24th was the second to the most. COA and front were machine ranked based on features that have demonstrated high correlation to ranks provided by the two human experts.

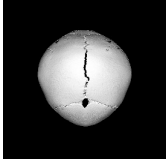
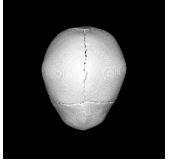
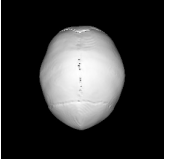
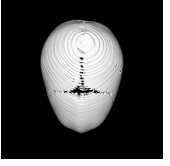
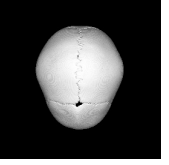
images					
COA	5	4	3	2	1 least
Expert1	7	3	5	4	1
Expert2	12	3	5	2	1
front	2	3	5	8	1

Figure 5.3: 5 metopic least shape-deformed skulls.

look at Fig. 5.5, where the horizontal axis shows the scoring values provided by the COA feature and the red crosses and blue asterisks show the rankings provided by Expert1 and Expert2, respectively. There is close agreement on the most or least scored skulls, but quite a lot of disagreement in between.

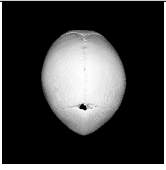
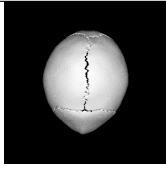
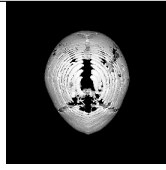
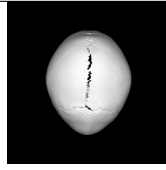
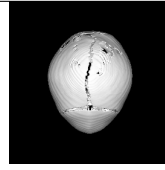
images					
COA	19	17	13	9	7
Expert1	9	22	16	15	13
Expert2	9	13	6	11	17
front	17	22	6	16	14

Figure 5.4: 5 metopic inconsistently ranked skulls

### 5.2.2 sagittal class

As shown in Table 5.2, the sagittal ranking orders from the two experts were moderately correlated at 0.5135. In contrast, a machine generated feature, back, correlated at 0.6512 to Expert1 and 0.5808, slightly less so, to Expert2. As shown on the left of Fig. 5.6, the more angular is the back of a sagittal skull, the more shape-deformed is the skull. Feature cmp2Circle is also correlated to the shape-deformity of a sagittal skull; the less circular is a sagittal skull, the more shape-deformed it is (as shown on the left of Fig. 5.6). Feature cmp2Mean correlated at 0.4937 to Expert1 and 0.4477 to Expert2. Feature w2l is a simple ratio of width over length of a skull. It has a negative correlation, therefore, to deformity; when the skull is narrower or longer in proportion (also shown on the left of Fig. 5.6), the ratio value is lower and the deformity is higher. Feature w2l had a negative correlation of -0.4436, moderately inversely correlated to Expert2 and only -0.3510 to Expert1.

In sagittal class, feature cmp2Mean is strongly correlated to features back (0.7889), feature cmp2Circle (0.9622) and w2l (-0.8830). Therefore, in general, the more deformed a sagittal skull is, the less it shapes like the mean control skull representation, the more angular it is at the back of its skull, the less circular it is, and the higher the width over length ratio value it has.

Figures 5.7, 5.8, and 5.9 show the five most deformed, five least deformed, and five of the middle group of sagittal skulls in order of ranking by the back feature and compared to

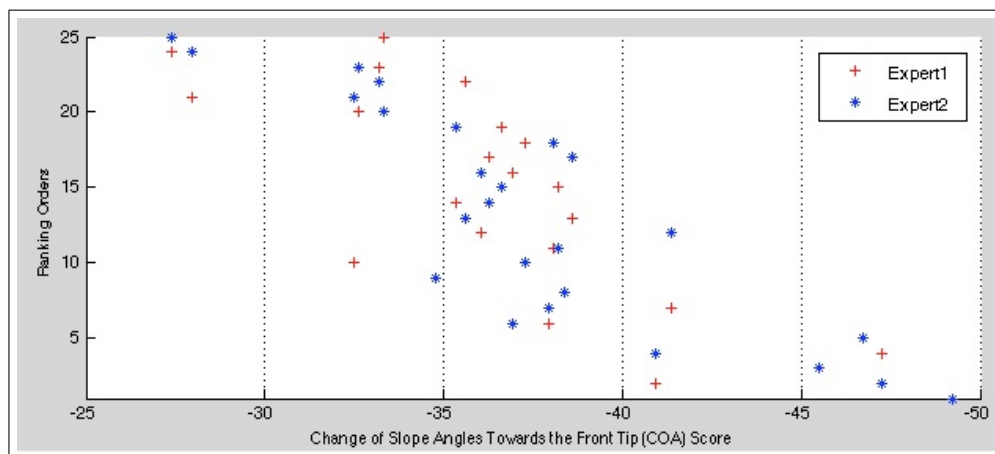


Figure 5.5: Ranking orders provided by the two experts in correlation to machine ranking measure, COA.

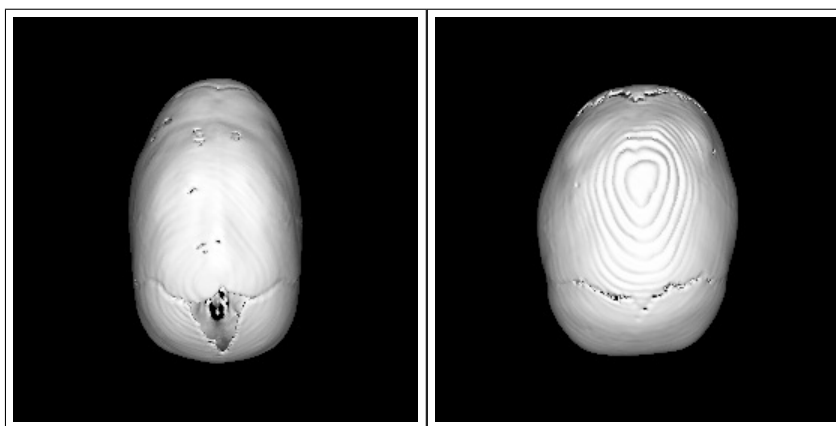


Figure 5.6: Illustration of a more shape-deformed sagittal skull (left), whose back is more angular, its width over length ratio is lower, and as a whole, it is less circular; whereas a less shape-deformed sagittal skull (right), whose back is less angular and as a whole, it is more circular and appears more like the mean control skull representation.

	Expert1	Expert2	back	cmp2Circle	cmp2Mean	w2l
Expert1	1	0.5135	0.6512	0.5190	0.4937	-0.3510
Expert2	0.5135	1	0.5808	0.4868	0.4477	-0.4436
back	0.6512	0.5808	1	0.8434	0.7889	-0.7584
cmp2Circle	0.5190	0.4868	0.8434	1	0.9622	-0.9450
cmp2Mean	0.4937	0.4477	0.7889	0.9622	1	-0.8830
w2l	-0.3510	-0.4436	-0.7584	-0.9450	-0.8830	1

Table 5.2: Correlation coefficients of sagittal ranking orders.

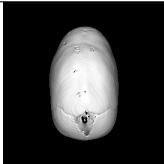

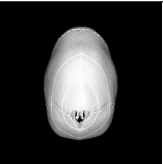


images					
back	57 most	56	55	54	53
Expert1	37	56	48	50	53
Expert2	50	57	15	20	36
cmp2Circle	56	57	45	54	52
cmp2Mean	53	56	40	57	50

Figure 5.7: 5 sagittal most shape-deformed ranks. Back, cmp2Circle and cmp2Mean are machine ranked based on features that have demonstrated high correlation to ranking orders from the two experts.

the cmp2Circle feature, Expert1, and Expert2. Again there is much more agreement in the top five and bottom five groups and much less in the middle, as one would expect.

### 5.2.3 unilateral coronal class

The unilateral coronal class was most challenging. When both right and left unilateral coronal skull images were analyzed together as one synostosis class, cmp2Mean was the only feature achieving above 0.4 correlation, at 0.4358 to Expert1; and -0.0208 to Expert2. The correlation between Expert1 and Expert2 was only 0.3165. The feature w2l showed

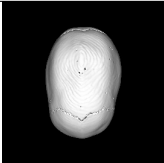
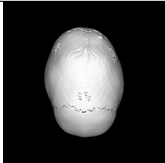
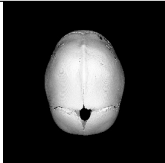
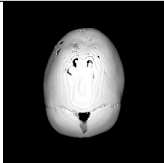
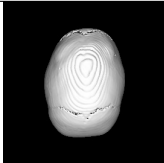
images					
back	5	4	3	2	1 least
Expert1	14	3	2	5	7
Expert2	24	8	7	4	2
cmp2Circle	33	4	1	2	5
cmp2Mean	29	6	1	2	4

Figure 5.8: 5 sagittal least shape-deformed ranks.

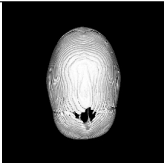

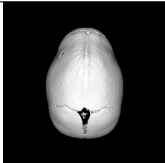
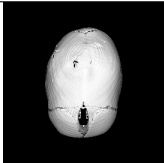
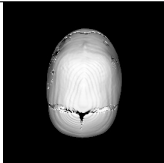
images					
back	47	40	38	23	11
Expert1	11	20	54	6	15
Expert2	37	43	53	23	1
cmp2Circle	43	40	23	16	21
cmp2Mean	43	41	18	14	20

Figure 5.9: 5 sagittal inconsistently ranked skulls.

a slightly higher correlation of 0.3470 to Expert1 and almost no correlation to Expert2. Similarly, feature symmetry showed a correlation of 0.3240 to Expert1 and hardly any to Expert2, as shown in table 5.3. The lack of correlation among the two experts suggests that the two experts used different definitions of shape-deformity to class rank the synostosis skulls.

It is worth noting that feature cmp2Mean is highly correlated to feature symmetry (0.6836) and feature w2l (0.6014). Therefore, in general, the more deformed an unilateral

coronal skull is, the less it appears like the mean control representation, the more asymmetrical it is, and the higher width over length ratio value it has.

	Expert1	Expert2	cmp2Mean	w2l	symmetry
Expert1	1	0.3165	0.4358	0.3470	0.3240
Expert2	0.3165	1	-0.0208	0.0810	-0.0469
cmp2Mean	0.4358	-0.0208	1	0.6014	0.6836
w2l	0.3470	0.0810	0.6014	1	0.0917
symmetry	0.3240	-0.0469	0.6836	0.0917	1

Table 5.3: Correlation results of uni-coronal ranking orders.

To better understand unilateral coronal synostosis class, we analyzed the 21 right uni-coronal and 12 left uni-coronal skull images separately as two subclasses.

**Right unilateral coronal class** When right unilateral coronal skulls were evaluated as a subclass alone, features cmp2Mean, w2l, and symmetry achieved higher correlation to Expert1 at 0.5024, 0.4305, and 0.3750 respectively, as shown in table 5.4. Nevertheless, the correlation between Expert1 and Expert2 dropped to 0.1195 from 0.3165 in Fig. 5.3.

Fig. 5.10 and Fig. 5.11 show the top five most deformed and top five least deformed right uni-coronal skulls in the order of ranking by the cmp2Mean feature and in comparison to the rankings of the w2l, and symmetry features and those assigned by Expert1 and Expert2. Here, the five sets of ranking orders are reasonably consistent, particularly between the orders from Expert1 and from the cmp2Mean feature.

**Left unilateral coronal class** When left unilateral coronal skulls were evaluated as a subclass alone, feature cmp2Mean achieved higher correlation to Expert1 at 0.4693 but w2l and symmetry features dropped to 0.1001 and 0.2180 respectively, as shown in table 5.5. Additionally, the correlation between Expert1 and Expert2 increased 100% to 0.6224 when it was evaluated as a subclass alone. The small sample size of 12 might contribute to this coincidental high correlations between the two human experts.

	Expert1	Expert2	cmp2Mean	w2l	symmetry
Expert1	1	0.1195	0.5024	0.4305	0.3750
Expert2	0.1195	1	-0.1737	0.0997	-0.2790
cmp2Mean	0.5024	-0.1737	1	0.6612	0.7300
w2l	0.4305	0.0997	0.6612	1	0.1746
symmetry	0.3750	-0.2790	0.7300	0.1746	1

Table 5.4: Correlation results of right uni-coronal ranking orders.

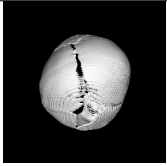
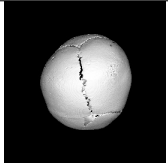
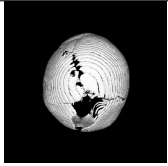
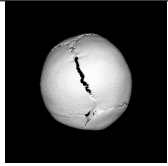
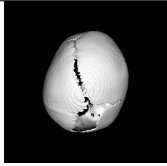
images					
cmp2Mean	21 most	20	19	18	17
Expert1	16	14	21	20	9
Expert2	3	18	1	19	2
w2l	16	17	14	19	8
symmetry	21	10	12	19	18

Figure 5.10: 5 right unilateral coronal most shape-deformed ranks. cmp2Mean, w2l and symmetry are machine ranked based on features that have demonstrated higher correlation to ranking orders from the two experts.

	Expert1	Expert2	cmp2Mean	w2l	symmetry
Expert1	1	0.6224	0.4693	0.1001	0.2180
Expert2	0.6224	1	0.3769	0.0270	0.2378
cmp2Mean	0.4693	0.3769	1	0.3207	0.7368
w2l	0.1001	0.0270	0.3207	1	-0.1250
symmetry	0.2180	0.2378	0.7368	-0.1250	1

Table 5.5: Correlation results of left uni-coronal ranking orders.



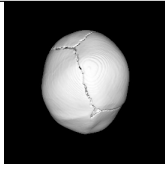
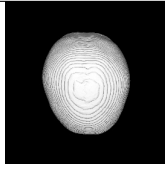
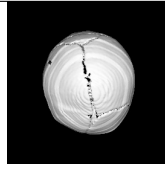
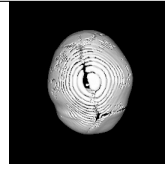
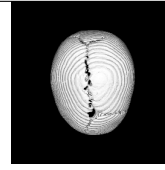
images					
cmp2Mean	5	4	3	2	1 least
Expert1	10	1	4	15	2
Expert2	5	16	7	4	15
w2l	4	3	10	1	2
symmetry	15	3	7	5	1

Figure 5.11: 5 right unilateral coronal least shape-deformed ranks.

### 5.3 Discussion

In severity assessment and class ranking, we have described a methodology for quantifying skull deformity using six attributes obtained from a projection of the top view of the skull of craniosynostosis subjects. Our methods are simple, yet powerful, allowing feature extraction even on low-quality CT images. Each of our features allows a score to be assigned to a skull indicating the degree of deformation according to that feature. In order to assess the utility of our features, we computed correlations between expert rankings of the skulls in each class and the rankings of our program with each feature. For the metopic class, two of our features, *change of average slope angle towards front tip* and *average slope angle of front tip*, were highly correlated with both expert rankings, which were also highly correlated to one another. For the sagittal class, there were medium-high correlations among three of our features, *average slope angle of back*, *compare to circle*, and *compare to mean unaffected*, and the experts, and a medium correlation between the two experts. For the unilateral coronal case, two of our features, *width to length ratio* and *symmetry*, achieved a low positive correlation with one of the experts, and the experts had a low positive correlation with each other. However, feature *compare to mean unaffected* of the right unilateral coronal subclass achieved medium correlation at 0.5025 to Expert1 even when the correlation between the

two experts was at 0.1195; and 0.4693 to Expert1 for the left unilateral coronal subclass. The experts received no prior training or instructions, which may account for some of their disagreement. Furthermore, the reason that the experts asked us to design computer algorithms was to provide a consistent and precise measure of the deformation. The process of comparing our rankings and those of the experts has produced a number of new insights that we will employ in designing and introducing new features and new scoring mechanisms.

## Chapter 6

## PRE-POST SURGERY CHANGE EFFECT EXPERIMENTS AND RESULTS

Based on the correlation results in Section 5.2, several useful features were identified and selected from each synostosis class. The features in the metopic class included *COA* and *front*. The features in the sagittal class included *back*, *cmp2Circle*, *cmp2Mean* and *w2l*. The features in the right unilateral coronal subclass included *cmp2Mean*, *w2l* and *symmetry*. Only one marginal feature, *cmp2Mean* was identified in the left unilateral subclass. All together, there were 7 selected features: *cmp2Mean*, *w2l*, *cmp2Circle*, *symmetry*, *front*, *back*, and *COA* to be used for learning and scoring purposes. The scoring features helped to quantify the pre-post surgery changes automatically, consistently and objectively.

To understand the pre-post surgery changes, the selected features in each class were used to analyze the post-surgery skull images by comparing them to their pre-surgery counterparts, as well as the entire collection of the unaffected skull images. There were 34 unaffected skull images in the dataset. Fig. 6.1 and Fig. 6.2 show the low and high bounds in each feature of the entire unaffected image set.

Although there were 115 pre-surgery images (25 of metopic, 57 of sagittal, 21 of right unilateral coronal, and 12 of left unilateral coronal) in the dataset, only 57 of them (15 of metopic, 21 of sagittal, 12 of right unilateral coronal, and 9 of left unilateral coronal) had a complete set of pre-surgery and post-surgery skull image pair. We will examine each class.

### 6.1 Metopic class

There were 15 pre- and post-surgery metopic synostosis skull pairs. Both *COA* and *front* features were used to score the pre- and post-surgery images. In Fig. 6.3, the post-surgery *COA* graph, shown in red, is below the pre-surgery *COA* graph, shown in blue. This indicates that 2 years after the surgery, every single subject had reduced its degree of deformity according to the *COA* feature measure. Both graph lines were sorted from less to

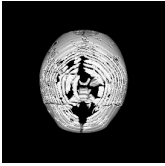
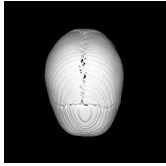
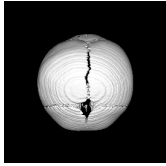
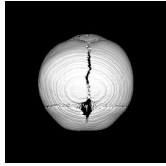
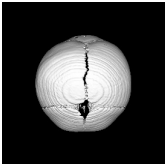
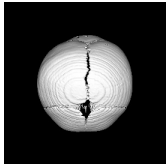
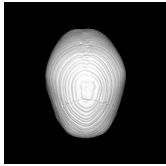
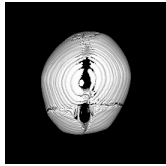
Feature	cmp2Mean	w2l	cmp2Circle	symmetry
Range (low)	1.75	0.681	2.74	0.787
Unaffected class				
Range (high)	8.24	0.94	12.24	8.813
Unaffected class				

Figure 6.1: The low and high bounds of features *cmp2Mean*, *w2l*, *cmp2Circle*, and *symmetry* in the unaffected class.

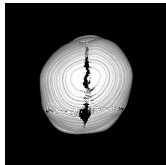
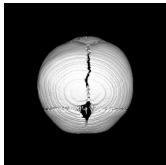
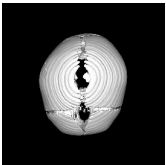
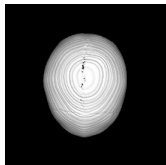
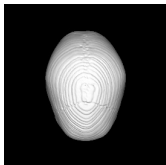
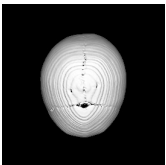
Feature	front	back	COA
Range (low)	6.28	28.42	-62.99
Unaffected class			
Range (high)	16.296	46.23	-49.98
Unaffected class			

Figure 6.2: The low and high bounds of features *front*, *back*, and *COA* in the unaffected class.

more severe based on the pre-surgery's *COA* scoring results. As the graphs move towards the right on the X-axis and the severity of the pre-surgery data increases, the gap between the two lines on the vertical axis widens. This implies that the more deformed the skull

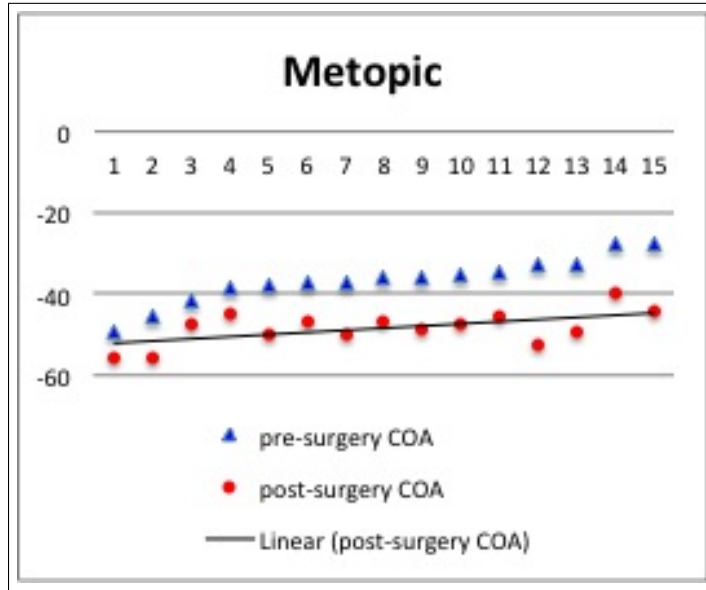


Figure 6.3: Horizontal axis indicates the deformity ranks, where 1 is the least and 15 is the most severe according to the scoring feature of *change of average slope angle towards front tip (COA)* in the metopic synostosis class.

was before the surgery, the more reduction in severity the skull experienced two years after the surgery. Subjects 12, 13 and 15 have the widest gaps between the pre- and post-surgery graph lines and based on their *COA* features scores, they are also the most deformed skulls prior to the surgery. On the contrary, subject 1, 3 and 4 have the narrowest gaps between their pre- and post-surgery graph lines and they are also the least deformed skulls prior to the surgery.

Very similar effects are shown in Fig. 6.4, where *front* feature scores were used instead of *COA*. Again, the entire post-surgery graph line, shown in red is below the pre-surgery graph line, shown in blue. Also similar to what was shown in the *COA* result above, the gap between the two lines widens and the change effect is stronger as the two lines move towards the right on the X-axis, where the severity of the pre-surgery skulls increase in deformity.

Fig. 6.5 shows the top five most deformed metopic skulls in the order of ranking by their pre-surgery *COA* feature scores, along with the severity change effects from their post-surgery scoring results.

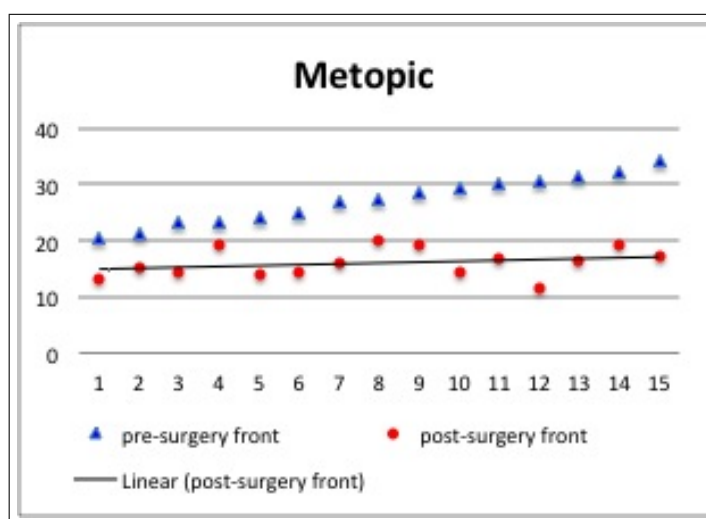


Figure 6.4: Horizontal axis indicates the deformity ranks, where 1 is the least and 15 is the most severe according to the scoring feature of *average slope angle of front tip (front)* in the metopic synostosis class.

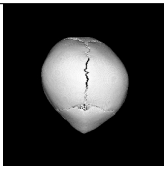
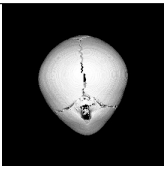
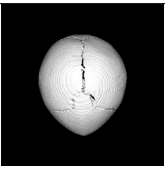
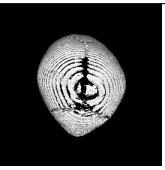
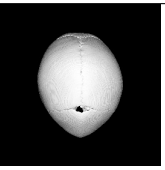
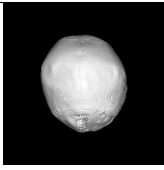
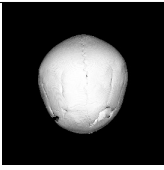
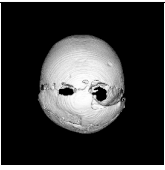
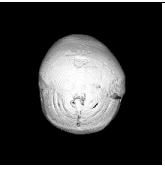
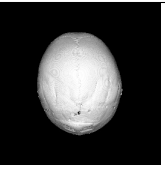
Severity rank	15	14	13	12	11
pre-surgery					
post-surgery					
COA	-61.51%	-43.20%	-52.08%	-61.95%	-30.22%
front	-49.87%	-31.78%	-50.53%	-62.97%	-45.17

Figure 6.5: 5 metopic most shape-deformed pre-surgery skulls according to their *COA* features scores. Pre-post change effects according to features *COA* and *front*.

According to the *COA* feature scores in Fig. 6.3, pre-surgery metopic skulls ranged from -49.23 (least severe) to -27.38 (most severe) and post-surgery metopic skulls ranged from

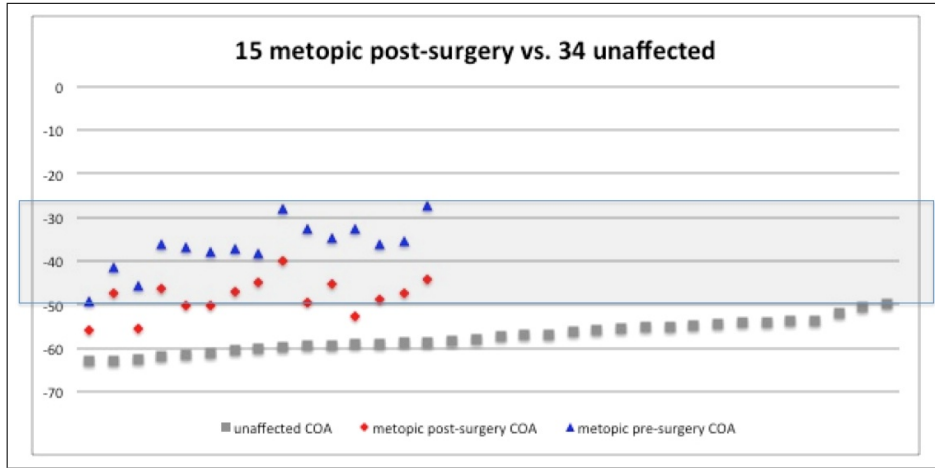


Figure 6.6: Vertical axis indicates the deformity measures according to the scoring feature of *change of average slope angle towards front tip (COA)* in the unaffected, the metopic post-surgery, and the metopic pre-surgery skulls. The grey shaded box shows where the deformity scores were out of the normal range. Note that all the pre-surgery skulls were out of the normal range.

-55.84 (least severe) to -40.06 (most severe). The deformity reduction varies from 13.44% to 61.95%. According to the *COA* feature scores in Fig. 6.6, the 34 unaffected skulls ranged from -62.99 to -49.98 while the 15 post-surgery skulls ranged from -55.84 (least severe) to -40.06 (most severe). There were 10 post-surgery metopic skulls scoring from -49.42 to -40.06, above -49.98, which is outside the normal range.

According to front feature scores in Fig. 6.4, pre-surgery metopic skulls ranged from 20.55 (least severe) to 34.34 (most severe) and post-surgery metopic skulls ranged from 11.38 (least severe) to 19.97 (most severe). The deformity reduction varies from 17.21% to 62.97%. According to the front feature scores in Fig. 6.7, unaffected skulls ranged from 6.28 to 16.296. There were 6 post-surgery metopic skulls scoring from 16.58 to 19.97, above 16.296, which is outside the normal range.

## 6.2 Sagittal class

There were 21 pre- and post-surgery sagittal synostosis skull pairs. All *back*, *cmp2Circle*, *cmp2Mean* and *w2l* features were used to score the pre- and post-surgery images. In Fig.

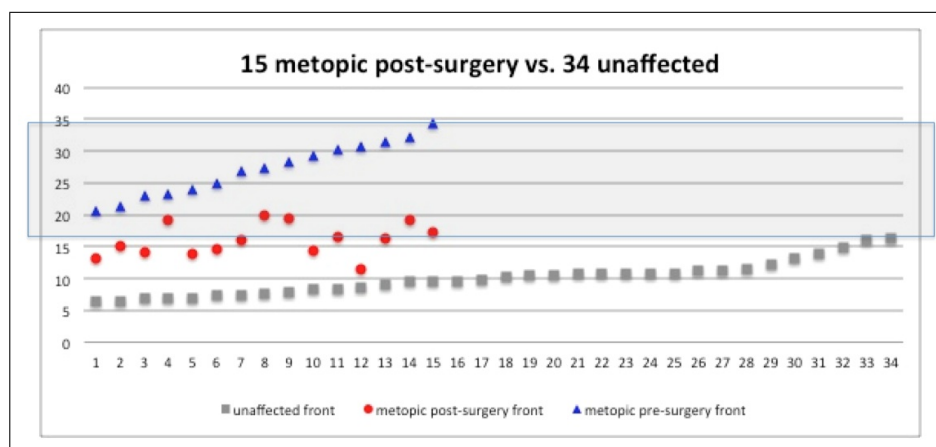


Figure 6.7: Vertical axis indicates the deformity measures according to the scoring feature of *average slope angle of front tip (front)* in the unaffected, the metopic post-surgery, and the metopic pre-surgery skulls. The grey shaded box shows where the deformity scores were out of the normal range. Note that all the pre-surgery skulls were out of the normal range.

6.8, the post-surgery *back* graph line, shown in red, is below the pre-surgery *back* graph line, shown in blue. This indicates 2 years after the surgery, according to the *back* feature measure, every single subject had reduced its degree of deformity. Both graph lines were sorted from less to more severe based on the back scoring results of the pre-surgery skull images. As the severity increases and both graphs move towards the right on the X-axis, the gap between the two lines on the vertical axis widens. This implies the more deformed the skull was before the surgery, the more reduction in severity the skull experienced two years after the surgery. Subjects 11, 17, 18 and 19 have the widest gaps between the pre- and post-surgery graph lines, and based on their *back* feature scores, they are also the most deformed skulls prior to the surgery. On the contrary, subjects 1, 2, 3, 7, 10 and 16 have the narrowest gaps between their pre- and post-surgery graph lines and 1, 2, 3, and 7 are also the least deformed skulls prior to the surgery. Very similar effects are shown in Fig. 6.9, where the *cmp2Circle* feature scores were used instead of *back*. Again, except for subject 4, the entire post-surgery graph line, shown in red is below the pre-surgery graph line, shown in blue. Also similar to what was shown in the *back* result above, the gap between the two lines widens as the two lines travel towards the right on the X-axis, where the severity of



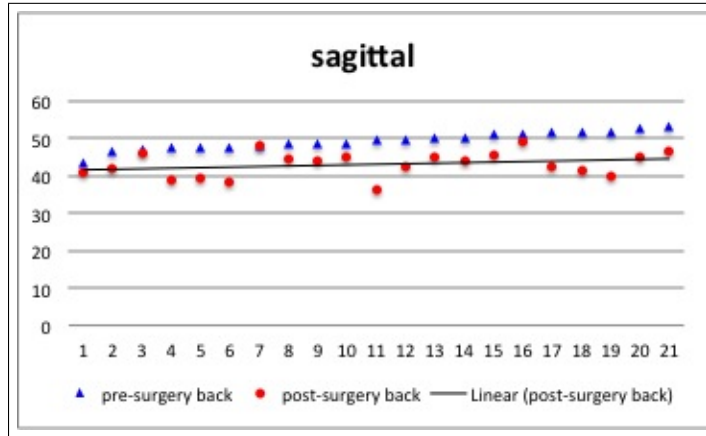


Figure 6.8: Horizontal axis indicates the deformity ranks, where 1 is the least and 21 is the most severe according to the scoring feature of *average slope angle of back (back)* in the sagittal class.

the pre-surgery skulls increase in deformity. Similar general conclusion can be drawn in Fig. 6.10, where *cmp2Mean* feature scores were used instead. However, subject 1 and subject 3 had higher deformity *cmp2Mean* feature scores on their post-surgery skulls than on their pre-surgery skulls. In Fig. 6.11, the post-surgery *w2l* graph line, shown in red is above the pre-surgery *w2l* graph line, shown in blue. This is because as a sagittal skull reduces in deformity, one of the indicators is having a more normal, or higher *w2l* ratio value.

Fig. 6.12 shows the top five most deformed sagittal skulls in the order of ranking by their pre-surgery *back* feature scores, along with the severity change effects from their post-surgery scoring results.

According to the *back* feature scores in Fig. 6.8, pre-surgery sagittal skulls ranged from 43.59 (least severe) to 53.31 (most severe) and post-surgery sagittal skulls ranged from 36.1 (least severe) to 48.8 (most severe). Subject by subject, there were improvements on every single skull after the surgery but the reduction of deformity varied between 0.3% and 27.24%. According to the *back* feature scores in Fig. 6.13, unaffected skulls ranged from 28.42 to 46.23. There were 3 post-surgery sagittal skulls scoring from 46.62 to 48.8, above 46.23, which is outside the normal range.

According to the *cmp2Circle* feature scores in Fig. 6.9, pre-surgery sagittal skulls ranged

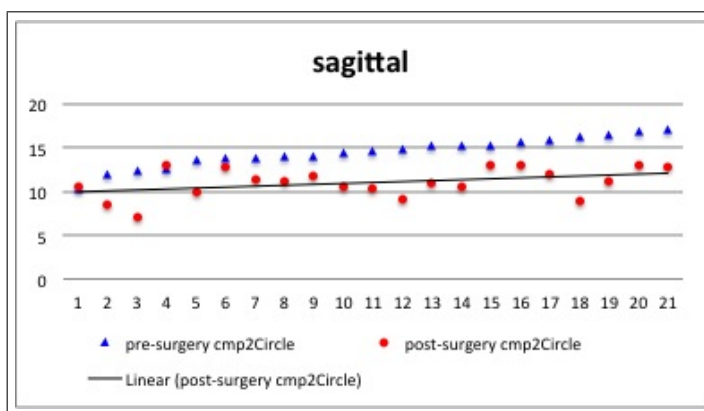


Figure 6.9: Horizontal axis indicates the deformity ranks, where 1 is the least and 21 is the most severe according to the scoring feature of *compare to circle* (*cmp2Circle*) in the sagittal class.

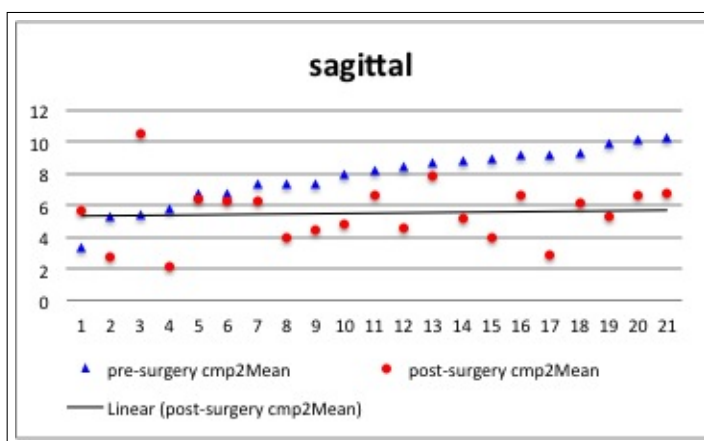


Figure 6.10: Horizontal axis indicates the deformity ranks, where 1 is the least and 21 is the most severe according to the scoring feature of *compare to mean unaffected* (*cmp2Mean*) in the sagittal class.

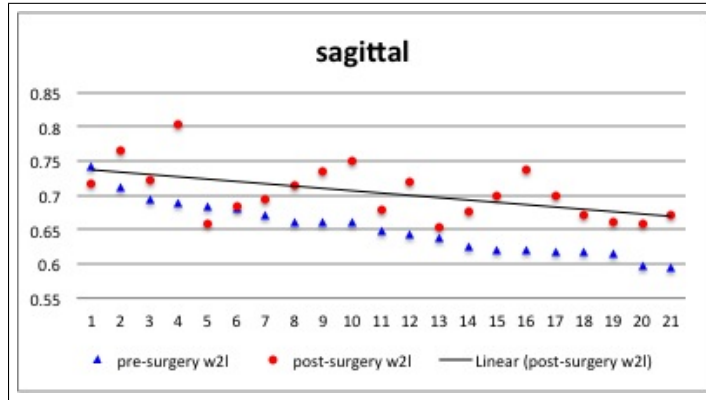


Figure 6.11: Horizontal axis indicates the deformity ranks, where 1 is the least and 21 is the most severe according to the scoring feature of *width to length ratio* (*w2l*) in the sagittal class.



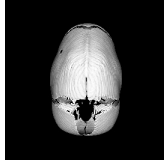
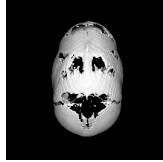


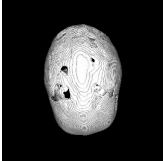
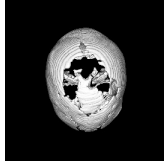
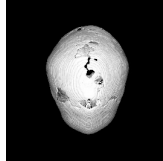
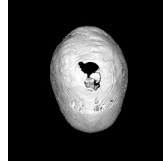
Severity rank	21	20	19	18	17
pre-surgery					
post-surgery					
back	-12.55%	-15.15%	-23.11%	-19.84%	-17.25%
cmp2Circle	-25.42%	-14.91%	-45.29%	-32.66%	-30.60%
cmp2Mean	-34.25%	-18.10%	-68.56%	-46.47%	-46.20%
w2l	10.22%	2.35%	18.87	12.61%	12.56%

Figure 6.12: 5 sagittal most shape-deformed pre-surgery skulls according to their *back* features scores. Score changes of features *back*, *cmp2Circle*, *cmp2Mean*, and *w2l* from each of these 5 pre-surgery skulls to its 2-year post-surgery status.

from 10.29 (least severe) to 17.08 (most severe) and post-surgery sagittal skulls ranged from 7.09 (least severe) to 13.06 (most severe). Subject by subject, the reduction of deformity

varied between 6% and 45%, but there were also 2 in which deformity increased by 2%. According to the *cmp2Circle* feature scores in Fig. 6.14, unaffected skulls ranged from 2.74 to 12.24. There were 6 post-surgery sagittal skulls scoring from 12.741 to 13.064, above 12.24, which is outside the normal range.

According to the *cmp2Mean* feature scores in Fig. 6.10, pre-surgery sagittal skulls ranged from 3.38 (least severe) to 10.22 (most severe) and post-surgery sagittal skulls ranged from 2.14 (least severe) to 10.45 (most severe). Subject by subject, the reduction of deformity varied between 6% and 68.56%, but there were also 2 cases of deformity increasing by 66% and 95%. In Fig. 6.15, unaffected skulls ranged from 1.75 to 8.24 according to the *cmp2Mean* feature scores and there was 1 post-surgery sagittal skull scoring at 10.45, above 8.24, which is outside the normal range.

According to the *w2l* feature scores in Fig. 6.11, pre-surgery sagittal skulls ranged from 0.595 (least severe) to 0.742 (most severe) and post-surgery sagittal skulls ranged from 0.652 (least severe) to 0.80 (most severe). Subject by subject, the reduction of deformity varied between 2% and 18.87% but there were also 2 cases of deformity increasing by 4%. According to the *w2l* feature scores in Fig. 6.16, unaffected skulls ranged from 0.68 to 0.94. There was 8 post-surgery sagittal skulls scoring from 0.679 to 0.652, below 0.68, which is outside the normal range.

### **6.3 Right unilateral subclass**

There were 12 pre- and post-surgery right unilateral coronal synostosis skull pairs. All *cmp2Mean*, *symmetry* and *w2l* features were used to score the pre- and post-surgery images.

In Fig. 6.17, the post-surgery *cmp2Mean* graph line, shown in red, is mostly below the pre-surgery *cmp2Mean* graph line, shown in blue. This indicates that 2 years after the surgery, according to the *cmp2Mean* feature measure, every single subject had reduced its degree of deformity. Both graph lines were sorted from less to more severe based on the pre-surgery *cmp2Mean* scoring results. As the severity increases and the two graph lines move towards the right on the X-axis, the gap between the two lines on the vertical axis widens. This implies that the more deformed the skull was before the surgery, the more the reduction in severity the skull experienced two years after the surgery. Subjects

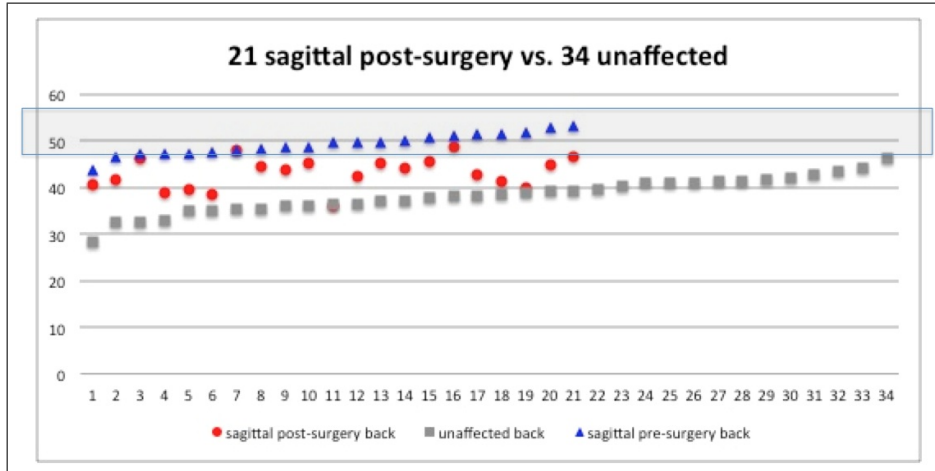


Figure 6.13: Vertical axis indicates the deformity measures according to the scoring feature of *average slope angle of back (back)* in the unaffected, the sagittal post-surgery, and the sagittal pre-surgery skulls. The grey shaded box shows where the deformity scores were out of the normal range. Note that almost all the pre-surgery skulls were out of the normal range.

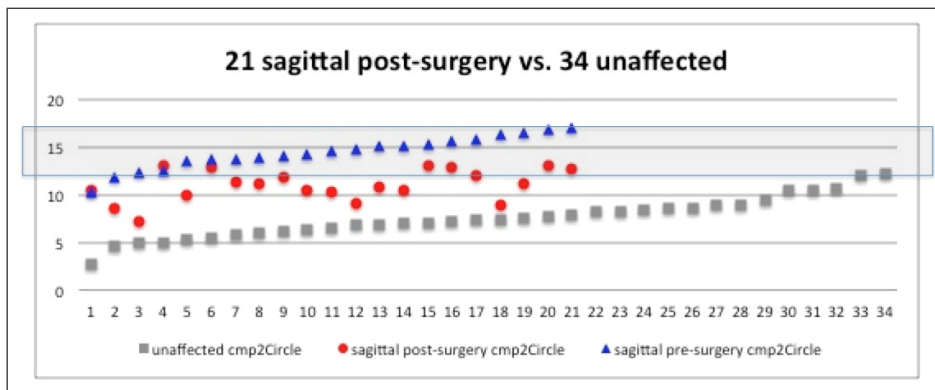


Figure 6.14: Vertical axis indicates the deformity measures according to the scoring feature of *compare to circle (cmp2Circle)* in the unaffected, the sagittal post-surgery, and the sagittal pre-surgery skulls. The grey shaded box shows where the deformity scores were out of the normal range. Note that almost all the pre-surgery skulls were out of the normal range.

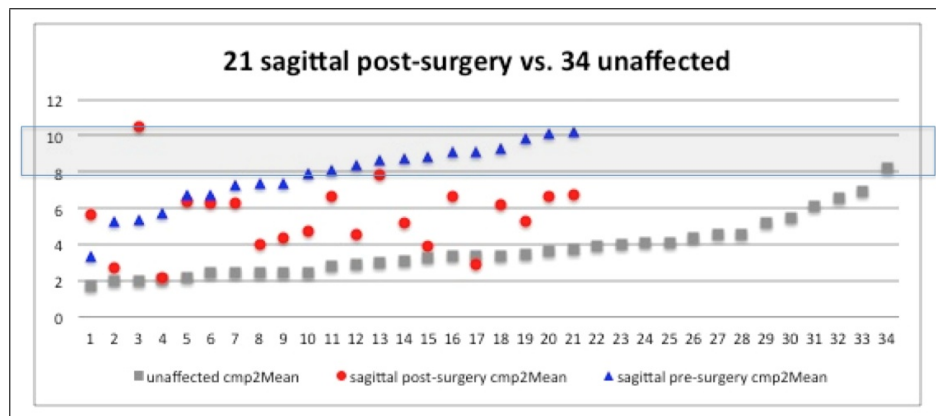


Figure 6.15: Vertical axis indicates the deformity measures according to the scoring feature of *compare to mean unaffected* (*cmp2Mean*) in the unaffected, the sagittal post-surgery, and the sagittal pre-surgery skulls. The grey shaded box shows where the deformity scores were out of the normal range. Note that almost half of the pre-surgery skulls were out of the normal range.

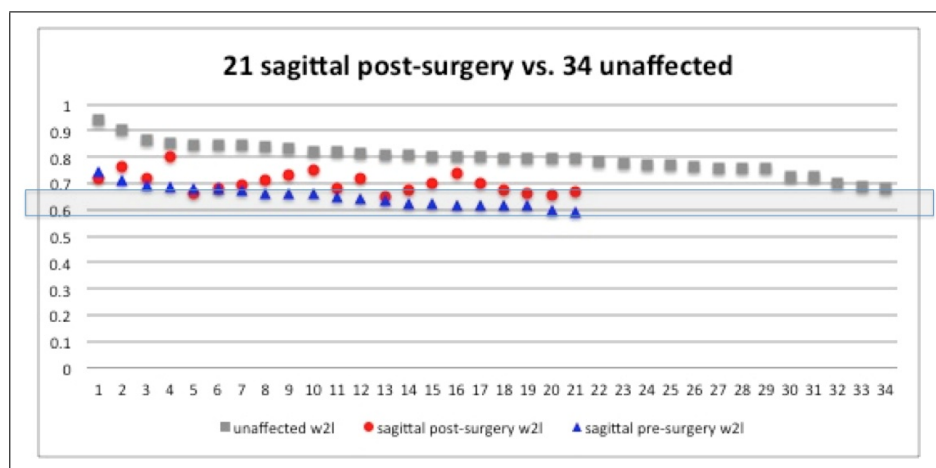


Figure 6.16: Vertical axis indicates the deformity measures according to the scoring feature of *width to length ratio* (*w2l*) in the unaffected, the sagittal post-surgery, and the sagittal pre-surgery skulls. The grey shaded box shows where the deformity scores were out of the normal range. Note that majority of the pre-surgery skulls were out of the normal range.

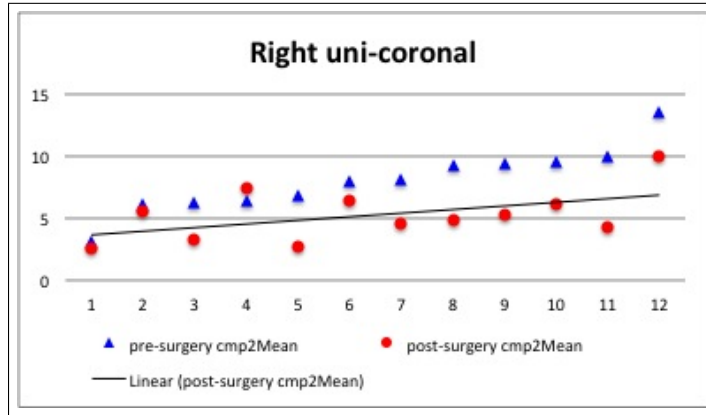


Figure 6.17: Horizontal axis indicates the deformity ranks, where 1 is the least and 12 is the most severe according to the scoring feature of *compare to mean unaffected (cmp2Mean)* in right unilateral coronal subclass.

11 and 8 have the widest gap between the pre- and post-surgery graph lines and based on their *cmp2Mean* features scores, they are also the most deformed skulls prior to the surgery. On the contrary, subjects 1, 2, and 6 have the narrowest gaps between their pre- and post-surgery graph lines and they are also the least deformed skulls prior to the surgery.

Very similar effects are shown in Fig. 6.18, where *symmetry* feature scores were used instead of *cmp2Mean*. The majority of the post-surgery graph line, shown in red is below the pre-surgery graph line, shown in blue. However, subjects 2, 3, 5 and 12 have higher severity scores on the post-surgery graph than on the pre-surgery graph line. Also similar to what was shown in the *cmp2Mean* result above, the gap between the two lines widens as the two lines travel towards the right on the X-axis.

Similar general conclusion can be drawn in Fig. 6.19, where *w2l* feature scores were used instead. However, subject 2 has a slightly higher deformity *w2l* feature score on its post-surgery graph line than on its pre-surgery graph line.

Fig. 6.20 shows the top five most deformed right unilateral coronal skulls in the order of ranking by their pre-surgery *cmp2Mean* feature scores, along with the severity change effects from their post-surgery scoring results.

According to the *cmp2Mean* feature scores in Fig. 6.17, pre-surgery right unilateral

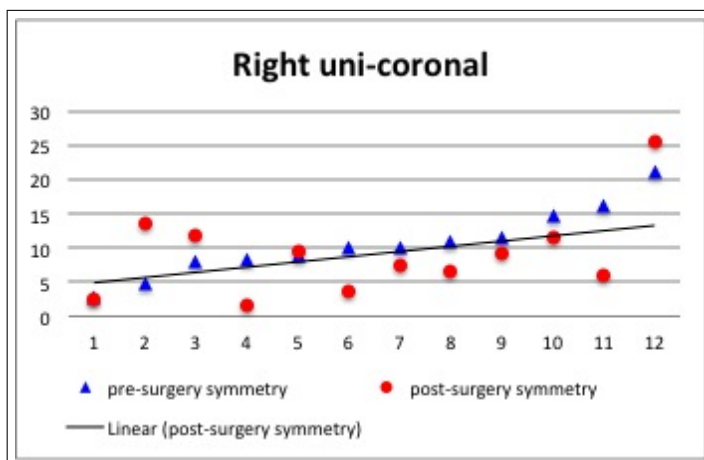


Figure 6.18: Horizontal axis indicates the deformity ranks, where 1 is the least and 12 is the most severe according to the scoring feature of *symmetry* in right unilateral coronal subclass.

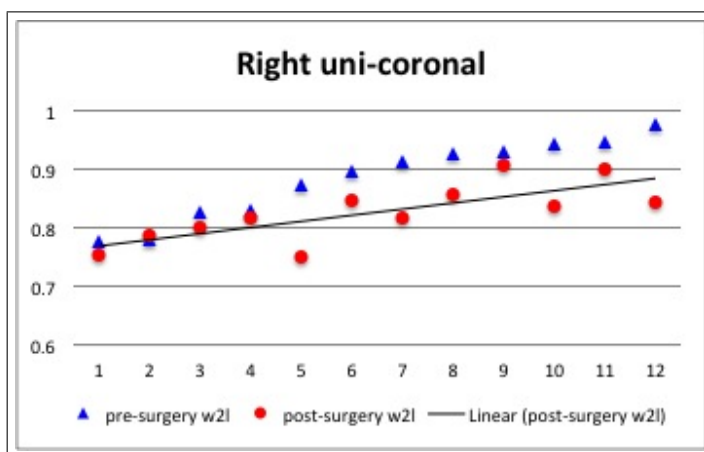


Figure 6.19: Horizontal axis indicates the deformity ranks, where 1 is the least and 12 is the most severe according to the scoring feature of *width to length ratio (w2l)* in right unilateral coronal subclass.



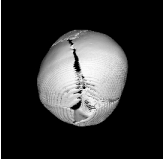
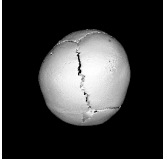
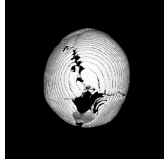
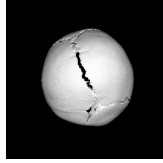
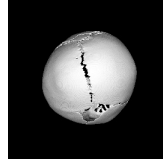
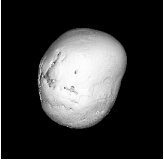
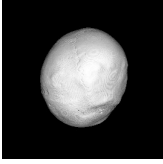
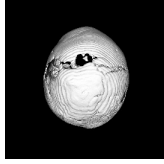
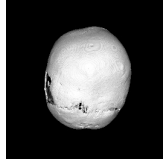
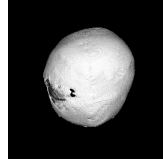
Severity rank	12	11	10	9	8
pre-surgery					
post-surgery					
cmp2Mean	-26.08%	-56.61%	-35.75%	-44.35%	-48.16%
symmetry	21.3%	-26.56%	-20.0%	-21.2%	-63.09%
w2l	-10.32%	-7.35%	-5.57%	-11.35%	-13.54%

Figure 6.20: 5 right unilateral coronal most shape-deformed pre-surgery skulls according to their *cmp2Mean* features scores. Score changes of features *cmp2Mean*, *symmetry*, and *w2l* from each of these 5 pre-surgery skulls to its 2-year post-surgery status.

coronal skulls ranged from 3.198 (least severe) to 13.513 (most severe), and post-surgery unilateral coronal skulls ranged from 2.593 (least severe) to 9.989 (most severe). Subject by subject, there were reduction in deformity varied from 8.41% to 61.07% but there was also one case of deformity increasing by 14.61%. According to the *cmp2Mean* feature scores in Fig. 6.21, unaffected skulls ranged from 1.75 to 8.24. There was one post-surgery right unilateral coronal skull scoring at 9.989, above 8.24, which is outside the normal range.

According to the *symmetry* feature scores in Fig. 6.18, pre-surgery right unilateral coronal skulls ranged from 2.69 (least severe) to 21.12 (most severe) and post-surgery unilateral coronal skulls ranged from 36.1 (least severe) to 48.8 (most severe). Change effects of reduction or increase in deformity varied from -81% (reduction) to 187.43% (increase). According to the *symmetry* feature scores in Fig. 6.22, unaffected skulls ranged from 0.787 to 8.813. There were 6 post-surgery right unilateral coronal skulls scoring from 9.198 to 25.621, above 8.813, which is outside the normal range.

According to the *w2l* feature scores in Fig. 6.19, pre-surgery right unilateral coronal

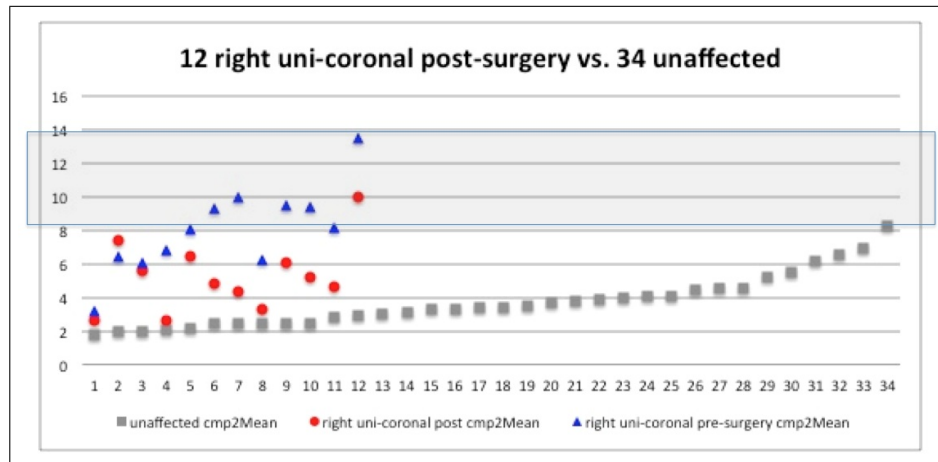


Figure 6.21: Vertical axis indicates the deformity measures according to the scoring feature of *compare to mean unaffected* (*cmp2Mean*) in the unaffected, the right uni-coronal post-surgery, and the right uni-coronal pre-surgery skulls. The grey shaded box shows where the deformity scores were out of the normal range. Note that half of the pre-surgery skulls were out of the normal range.

skulls ranged from 0.775 (least severe) to 0.975 (most severe) and post-surgery unilateral coronal skulls ranged from 0.749 (least severe) to 0.905 (most severe). Change effects of reduction or increase in deformity varied from 0.77% to -14.30%. According to the *w2l* feature scores in Fig. 6.23, the unaffected skulls ranged from 0.681 to 0.94. There was no post-surgery right unilateral coronal skulls scoring outside the normal range.

#### 6.4 Left unilateral subclass

There were 9 pre- and post-surgery left unilateral coronal synostosis skull pairs. Feature *cmp2Mean* was used to score the pre- and post-surgery images.

As shown in Fig. 6.24, 4 out of 9 post-surgery samples, shown in red are above the pre-surgery samples, shown in blue. This implies that according to the feature *cmp2Mean* scores, some skulls became more deformed 2 years after the surgery. Nevertheless, the general trend that was observed in the metopic, sagittal and right unilateral coronal skulls was also noted here. In general, the improvement after the surgery was measured to be higher on those skulls that were more severe before the surgery to begin with.

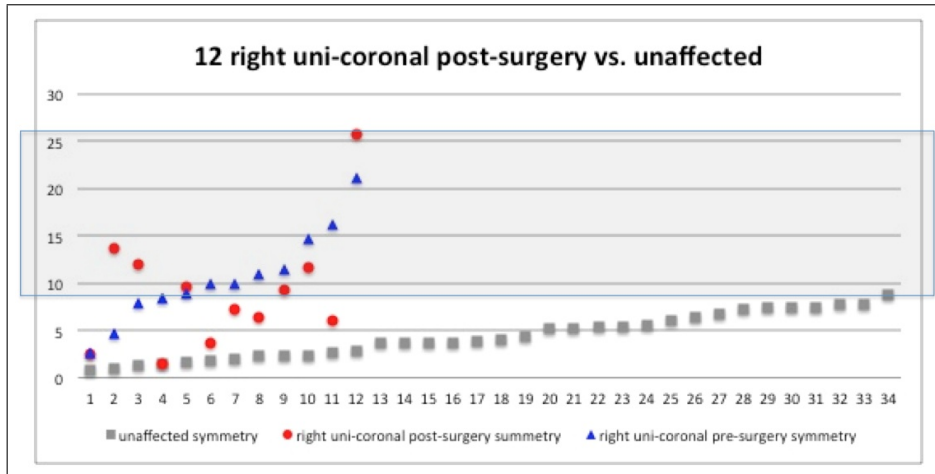


Figure 6.22: Vertical axis indicates the deformity measures according to the scoring feature of *symmetry* in the unaffected, the right uni-coronal post-surgery, and the right uni-coronal pre-surgery skulls. The grey shaded box shows where the deformity scores were out of the normal range. Note that more than half of the pre-surgery skulls were out of the normal range.

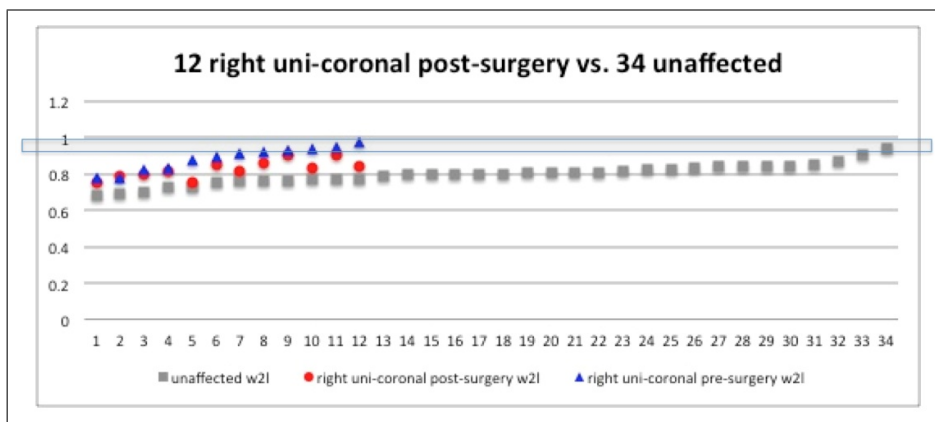


Figure 6.23: Vertical axis indicates the deformity measures according to the scoring feature of *width to length ratio (w2l)* in the unaffected, the right uni-coronal post-surgery, and the right uni-coronal pre-surgery skulls. The grey shaded box shows where the deformity scores were out of the normal range. Note that one third of the pre-surgery skulls were out of the normal range.

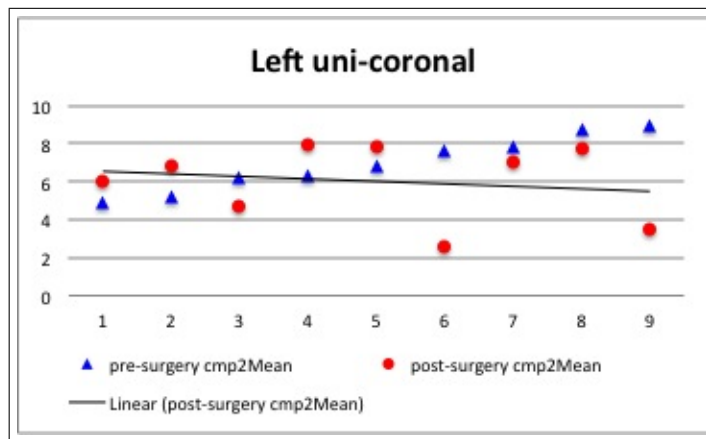


Figure 6.24: Horizontal axis indicates the deformity ranks, where 1 is the least and 9 is the most severe according to the scoring feature of *compare to mean unaffected (cmp2Mean)* in left unilateral coronal subclass.

In Fig. 6.25, unaffected skulls ranged from 1.75 to 8.24 according to the *cmp2Mean* feature scores and there was no post-surgery left unilateral coronal skulls scoring outside the normal range.

## 6.5 Discussion

In the *pre-post surgery change effect* module, we have described an approach for quantifying the surgery change effect using seven attributes obtained from a projection of the top view of the skull of craniosynostosis subjects before the surgeries, then again 2 years after the surgeries and also of the unaffected subjects. Each of our features allows a score to be assigned to a skull indicating the degree of deformation according to that features. For the metopic class, two of our features, *change of average slope angle towards front tip* and *average slope angle of front tip*, were highly correlated with both expert rankings were used to study the surgery change effect. For the sagittal class, four features, *average slope angle of back*, *compare to circle*, *compare to mean unaffected*, and *width to length ratio* were used for the study instead. For the right unilateral coronal subclass, three features, *compare to mean unaffected*, *width to length ratio*, and *symmetry* were considered most suitable. For the left unilateral coronal subclass, feature *compare to mean unaffected* was the only one

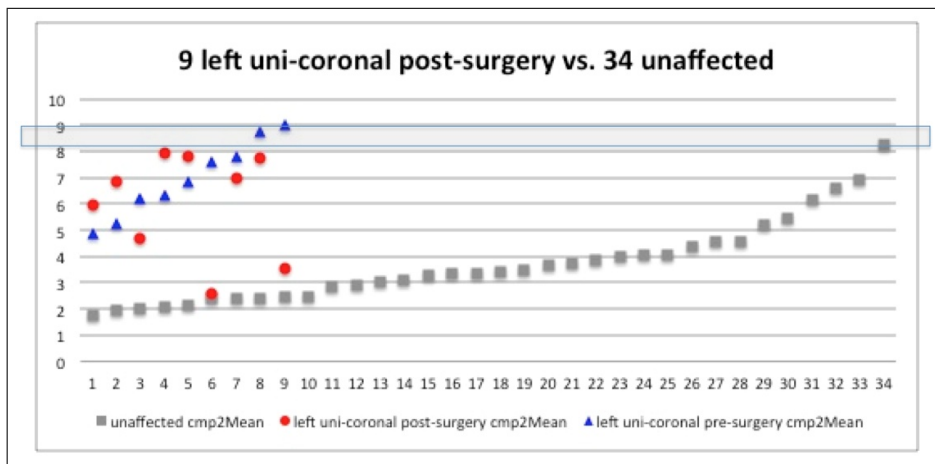


Figure 6.25: Vertical axis indicates the deformity measures according to the scoring feature of *compare to mean unaffected* (*cmp2Mean*) in the unaffected, the left uni-coronal post-surgery, and the left uni-coronal pre-surgery skulls. The grey shaded box shows where the deformity scores were out of the normal range. Note that two of the pre-surgery skulls were out of the normal range.

being considered as marginal suitable. Unlike the metopic class, the sagittal class, and the unilateral coronal subclass, of which the studies of pre-post change effect were concise, the experiment of the left unilateral coronal subclass was challenging and the result was inconclusive. Based on our experimental results alone, we can neither state objectively that the left unilateral coronal skulls have improved uniformly across nor are able to report quantitatively how much they have changed as a subclass.

## Chapter 7

### DISCUSSION, CONCLUSION, AND FUTURE WORK

The contributions of this thesis include:

1. optimizing the inclusion of prior acquired CT skull images,
2. introducing a new set of feature-engineering algorithms,
3. designing a general set of features for new quantification and scoring measures,
4. demonstrating these features with classification tasks,
5. demonstrating these features with severity assessment and class-ranking tasks, and
6. demonstrating these features with a pre-post surgery change analysis task.

#### **7.1 Study limitations and challenges**

Numerous limitations and challenges, some technical and some not, were encountered during our studies. All obstacles were tackled and the key ones were addressed and resolved. First, unlike the recent scans from the latest modern CT technology, the skull images used in our experiments were acquired more than seven years ago. Noise, holes and other imperfections were common on these older scan images. The dataset has been tremendously invaluable to our study, yet it was challenging to work with. The path in gathering data, integrating it, cleaning it, pre-processing it, trying it out, then rejecting or accepting it to be used in our studies has been time consuming, and occasionally difficult as well. Our intent was to use as many images from as many subjects as possible. Yet finding a way to overcome the noise and imperfections without altering the shape-characteristics of the skull images has been an iterative trial-by-error experiment. Committing to use the raw images as they

were originally generated was both a challenge and a contribution towards our automation goal. Translating an imperfect 3D skull image into a 2D contour so that the 3D shape characteristic of the skull can be preserved, described and analyzed was our response to the ultimate project objective. At the end, we were able to design domain-specific features and verify them on over 150 craniosynostosis skull images, in which many were disqualified and dismissed previously because of their poor scan quality. Second, the size of the 57 pre-post pair dataset (15 of metopic, 21 of sagittal, 12 of right unilateral coronal, and 9 of left unilateral coronal class) was small. Even though we had 57 sagittal pre-surgery skull images to start with, only 21 of them had a complete pre-post image set. Good engineering can never make up for the lack of data but we put our good faith in the data that we did have and proceeded forward with them. Third, the single-plane projection-based exterior contouring technique limited the full utilization of a 3D image. For instance, even though the contour could effectively capture the far-most protrusions in the skull, the indentations behind the protrusions were hidden and left out in the 2D exterior contour. Consequently, the selected features could not describe, analyze and rank what were not on the contour representations. Therefore, our tasks did not completely reflect the performance of the features. Fourth, the single-plane 2D contour restricted the development of some more powerful features. In order to describe a 3D skull for truly three-dimensional quantitative analysis, features that are unique to the multiple-plane contours along the superior-inferior axis should be implemented. Fifth, ideally, instead of marking the landmark points nasion and opisthion by hand, the landmarking module would have been automated to further promote objectivity, consistency and efficiency. Sixth, the different definitions of deformity used to assess severity by the two experts, a pediatrician and a surgeon, may account for some of their disagreement.

## **7.2 Conclusions**

We accomplished our three aims. First, we tested our new features on classification tasks and also compared their performance to previous research. In spite of their simplicity, the classification accuracy of our new features was significantly higher than previous results on head CT scan data from the same research studies. Second, we proposed a set of

features derived from CT scans of the skull that could be used to quantify the degree of abnormality of the disorder. A thorough set of experiments was used to evaluate the features as compared to two human craniofacial experts in a ranking evaluation. Our methods were simple, yet powerful, allowing feature extraction even on low-quality CT images. Third, we studied pre-post surgery change based on selected features we used in quantifying the severity of deformity of the disorder. Using the same selected features, we also compared and contrasted post-surgery craniosynostosis skulls to the unaffected class. For the metopic class, two of our features, *change of average slope angle towards front tip* and *average slope angle of front tip*, which were highly correlated with both expert rankings were used to study the surgery change effect. For the sagittal class, four features, *average slope angle of back*, *compare to circle*, *compare to mean unaffected*, and *width to length ratio* were used for the study instead. For the right unilateral coronal subclass, three features, *compare to mean unaffected*, *width to length ratio*, and *symmetry* were considered most suitable. For the left unilateral coronal subclass, feature *compare to mean unaffected* was the only one being considered as marginal suitable.

The results from our experiments were very promising not just for the classification experiment but in assessing the severity of a skulls deformation caused by craniosynostosis and measuring the change effects from corrective surgery. In addition, the process of comparing our rankings and those of the experts has produced a number of new insights that we have employed in designing new features and new scoring mechanisms. The purpose of the computer algorithms was to provide a consistent, non-subjective, and precise measure of the deformation.

### **7.3 Future work**

Many improvements could be tried and considered but we will list three that we consider as most promising. First, in order to create a set of features to more fully describe a 3D skull, the projection-based exterior contouring technique needs to be expanded from single-plane to multiple-plane along the superior-interior axis. Constrained by a single projection-plane, the granularity, locality, angularity and symmetry details in any salient point or in between salient points risk being undiscovered or under represented. Once the projection-based



contouring is expanded from single-plane to multiple-plane, additional features could be learned and designed. For instance, vertical angle features along the meridians of this 3D contour avatar could be added, scored and compared between an unaffected and an affected classes. Since each plane is a projection reflection of a much finer interval along the superior-interior axis, indentations and protrusions could be captured independently on each plane. The more details being fed and captured in the contours, the richer and more complete features can be customarily designed. As a result, the deeper and stronger meaning the feature scores can convey in the tasks we have in hands. Second, in the spirit of continuous improvement, all features we developed could be enhanced and optimized further. However, the author is particularly disappointed in the lower than expected effectiveness of the feature *symmetry* and would offer a few change recommendations. For instance, instead of comparing the average distance radius from the center between the entire left and the right contours of a skull, the average comparison could be more selective and localized to some specific contour segments. Another consideration is adding angular comparison to the *symmetry* feature in addition to average distance radius comparison. Third, the *cmp2Mean* feature was weak and under-utilized in this work. Given that there were 34 skull images in the unaffected dataset and wide scoring ranges were recorded in this control group, the author recommends examining the entire unaffected class more closely and also, building a multi-plane 3D mean unaffected contour representation as a comparison baseline instead. Furthermore, feature *cmp2Mean* could be expanded to allow more and better computation comparison between this mean representation and a synostosis class. Currently, only the average distance radius was computed in a mean control contour in order to baseline a subject skull contour. Other computations like angle and angular change can be added to improve the comparison.

## BIBLIOGRAPHY

- [1] J.C. Gower. Generalized procrustes analysis. *Psychometrika*, 40(1):33–51, 1975.
- [2] F.J. Rohlf and D. Slice. Extensions of the procrustes method for the optimal superimposition of landmarks. *Systematic Biology*, 39(1):40, 1990.
- [3] F. Bookstein. Landmark methods for forms without landmarks: morphometrics of group differences in outline shape. *Medical Image Analysis*, 1(3):225–243, January 3 1997.
- [4] S. Yang, L. Shapiro, M. Cunningham, M. Speltz, and SI Lee. Classification and feature selection for craniosynostosis. In *ACM-BCB*, 2011.
- [5] BJ. Slater, KA. Lenton, MD. Kwan, DM. Gupta, DC. Wan, and MT. Logaker. Cranial sutures: a brief review. *Plast. Reconstr. Surg.*, 121(4):170e–178e, April 2008.
- [6] J. Panchal and V. Uttchin. Management of craniosynostosis. *Plast. Reconstr. Surg.*, 111(6):2032–48, May 2003.
- [7] DT. Gault, D. Renier, D. Marchac, and BM Jones. Intracranial pressure and intracranial volume in children with craniosynostosis. *Plast. Reconstr. Surg.*, 90(3):377–81, September 1992.
- [8] Carlos Mendoza, Nabile Safdar, Kazunori Okada, Emmarie Myers, Gary F. Rogers, and Marius George Linguraru. Personalized assessment of craniosynostosis via statistical shape modeling. *Medical Image Analysis*, 18:635 – 646, 2014.
- [9] Marcelo Elias de Oliveira, Harri Hallila, Antti Ritvanen, Philippe Buchler, Mervi Paulasto, and Jyri Hukki. Feature-invariant image registration method for quantification of surgical outcomes in patients with craniosynostosis: a preliminary study. *Journal of Pediatric Surgery*, 46(E1 - E8), 2011.
- [10] Jeffrey R. Marcus, Leahthan F. Domeshek, Rajesh Das, Sean Marshall, Roger Nightingale, Tracey Stokes, and Srinivasan Mukundan. Objective three-dimensional analysis of cranial morphology. *Journal of Plastic Surgery*, 2008.
- [11] S. Ruiz-Correa, R.W. Sze, H.J. Lin, L.G. Shapiro, M.L. Speltz, and M.L. Cunningham. Classifying craniosynostosis deformations by skull shape imaging. *18th IEEE Symposium on Computer-Based Medical Systems*, pages 335–340, 2005.

- [12] H. Jill. Lin, Salvador. Ruiz-Correa, Raymond W. Sze, Michael L. Cunningham, Matthew. Speltz, Anne V. Hing, and Linda G. Shapiro. Efficient symbolic signatures for classifying craniosynostosis skull deformities. *Proceedings of the Workshop on Computer Vision for Biomedical Image Applications*, pages 302–313, October 2005.
- [13] I. Atomsukarto, L.G. Shapiro, J.R. Starr, C. Heike, B. Collett, M. Cunningham, and M.L. Speltz. 3d head shape quantification for infants with and without deformational plagiocephaly. In *Cleft Palate Craniofac J.*, volume 47(4), pages 368–377, 2010.
- [14] S.R. Lele and J.T Richtsmeier. An invariant approach to the statistical analysis of shapes. In *New York: Chapman and Hall/ CRC*, 2001.
- [15] S. Ruiz-Correa, D. Gatica-Perez, H.J. Lin, and L.G. Shapiro. A bayesian hierarchical model for classifying craniofacial malformations from ct imaging. In *30th Annual International IEEE EMBS conference*, 2008.
- [16] K. Aldridge, ID. George, and Cole KK. Facial phenotypes in subgroups of prepubertal boys with autism spectrum disorders are correlated with clinical phenotypes. *Molecular Autism*, 2:15–26, 2011.
- [17] Phillip Mitteroecker. Advances in geometric morphometrics. *Evol Biol*, 36:235–247, 2009.
- [18] T. Hutton. *Dense Surface Models of the Human Face*. PhD thesis, University College London, Gower Street, London, WC1E 6BT UK, September 2004.
- [19] P. Hammond, C. Forster-Gibson, and AE. Chudley. Face-brain asymmetry in autism spectrum disorders. *Molecular Psychiatry*, 13:614–623, 2008.
- [20] Peter. Hammond, Tim J. Hutton, Judith E. Allanson, Linda E. Campbell, Raoul C.M. Hennekam, Sean. Holden, Michael A. Patton, Adam. Shaw, I. Karen. Temple, Matthew. Trotter, Kieran C. Murphy, and Robin M. Winter. 3d analysis of facial morphology. *American Journal of Medical Genetics*, 126A:339–348, 2004.
- [21] Yaser S. Abu-Mostafa, Malik Magdon-Ismail, and Hsuan-Tien Lin. *Learning From Data*. AMLbook.com, 2012.
- [22] L. Heutte, T. Paquet, J. V. Moreau, Y. Lecourtier, and C. Olivier. A structural/statistical feature based vector for handwritten character recognition. *Pattern Recognition*, 19(7):629 – 641, 1998.
- [23] M. Shi, Y. Fujisawa, T. Wakabayashi, and F. Kimura. Handwritten numeral recognition using gradient and curvature of gray scale image. *Pattern Recognition*, 35(10):2051 – 2059, 2002.

- [24] S. Tsuruoka. Handwritten kanji and hiragana character recognition using weighted direction index histogram method. *IEICE Japan*, J70-D(7):1390 – 1397, 1987.
- [25] M. Yasuda and H. Fujisawa. An improvement of correlation method for character recognition. *IEICE Japan*, J62-D(3):217 – 224, 1979.
- [26] I. Lam, M. Cunningham, M. Speltz, and L. Shapiro. Classifying craniosynostosis with a 3d projection-based feature extraction system. *IEEE 27th International Symposium On Computer-Based Medical Systems*, May 2014.
- [27] L. Massimi and Massiomo Caldarelli. Isolated sagittal craniosynostosis: definition, classification and surgical indications. In *Childs Nerv Syst*, volume 28, pages 1311–1317, 2012.
- [28] L. Shapiro, K. Wilamowska, I. Atomsukarto, J. Wu, C. Heike, M. Speltz, and M. Cunningham. Shape-based classification of 3d head data. pages 692 – 700. ICIAP, 2009.
- [29] New Zealand University of Waikato. <http://www.cs.waikato.ac.nz/ml/weka/>. free software available under the GNU General Public License.
- [30] SM. Myers, CP. Johnson, and American Academy of Pediatrics Council on Children With Disabilities. Management of children with autism spectrum disorders. *Pediatrics*, 120(5):162–82, November 2007.
- [31] Centers for disease control and prevention. <http://www.cdc.gov/ncbddd/autism/data.html>.
- [32] <http://www.3dmd.com/>.
- [33] WE. DeMyer, W. Zeman, and CG. Palmer. The face predicts the brain: diagnostic significance of median facial anomalies for holoprosencephaly. *Pediatrics*, 34:256–263, 1964.
- [34] JH. Miles, TN. Takahashi, and J. Hong. Development and validation of a measure of dysmorphology: Useful for autism subgroup classification. *Am J Med Genet A*, 146:1101–1116, 2008.
- [35] A. Coates and A Ng. The importance of encoding versus training with sparse coding and vector quantization. *ICML*, 2011.
- [36] S.I. Lee, H. Lee, P. Abbel, and A.Y. Ng. Effective l1 regularized logistic regression. *Proceedings of The 21st National Conference on Artificial Intelligence*, 2006.
- [37] R. Tibshirani, M. Saunders, S. Rosset, Y. Heights, J. Shu, and K. Knight. Sparsity and smoothness via the fused lasso. *J. R. Statist. Soc.*, B(67):91–108, 2005.

- [38] R. Tibshirani. Regression shrinkage and selection via the lasso. *Journal of the Royal Statistical Society*, (58):267–288, 1996.
- [39] P. Kinahan. Multimodality pet/ct imaging, October 2011.
- [40] S. Yang, L. Shapiro, M. Cunningham, M. Speltz, C. Birgfeld, I. Atomsukarto, and SI Lee. Skull retrieval for craniosynostosis using sparse logistic regression models. *Proceedings of the MICCAI Workshop on Medical Content Based Retrieval for Clinical Decision Support*, Springer, 2012.
- [41] E. Mercan and L. Shapiro. Discriminative pseudo-landmark selection via l1-regularized logistic regression.
- [42] S. Liang, J. Wu, S. Weinberg, and L. Shapiro. Detection of landmarks on 3d human face data via deformable transformation. Submitted to IEEE ISBI 2013.
- [43] K. Wilamowska, L. Shapiro, and C. Heike. Classification of 3d face shape in 22q11.2 deletion syndrome. *ISBI'09 Proceedings of the Sixth IEEE international conference on Symposium on Biomedical Imaging: From Nano to Macro*, pages 534–537, April 2009.
- [44] J.C. Kolar and E.M. Salter. Craniofacial anthropometry: Practical measurement of the head and face for clinical, surgical, and research use. 1997.
- [45] Visualization toolkit, January 8 2011.

## VITA

Irma Lam received her Bachelor of Science in Electrical Engineering from University of Washington, her Master of Science in Electrical Engineering from UCLA, her MBA from Seattle University. Prior to her PhD training, she was Engineering Product Development Director and Program Director at Medtronic for over 6 years. She is currently a PhD candidate in Biomedical and Health Informatics, School of Medicine at the University of Washington, also a research assistant in Computer Science and Engineering department.